

AD 748223



GULF ELECTRONIC SYSTEMS

Gulf-EL-A12250

SEMIANNUAL TECHNICAL REPORT FOR THE PERIOD JANUARY 1, 1972 TO JUNE 30, 1972

CARBON RESEARCH

Sponsored by
Advanced Research Projects Agency
Arlington, Virginia
ARPA Order No. 1861

August 25, 1972

SEE AD 740764



R. J. Akins, J. L. Kaa, K. Koyama, R. J. Ptica, F. J. Schoen,
and J. C. Bokros (P.I.) (714-453-1000)

GULF OIL CORPORATION
GULF ENERGY & ENVIRONMENTAL SYSTEMS COMPANY
San Diego, California 92112

Program Code Number: 1D10

Contract Date: June 26, 1971

Contract Amount: \$226,235

Expiration Date: June 25, 1973

This research was supported by the Advanced Research Projects Agency of the Department of Defense under Contract No. DAHC15-71-C-0282.

"The views and conclusions contained in this document are those of the authors and should not be interpreted as necessarily representing the official policies, either expressed or implied, of the Advanced Research Projects Agency or the U.S. Government."

Reproduced by
NATIONAL TECHNICAL
INFORMATION SERVICE
U S Department of Commerce
Springfield VA 22151

DISTRIBUTION STATEMENT A

Approved for public release;
Distribution Unlimited

GULF ELECTRONIC SYSTEMS

A DIVISION OF GULF ENERGY & ENVIRONMENTAL SYSTEMS COMPANY
P.O. BOX 608, SAN DIEGO, CALIFORNIA 92112

DISCLAIMER NOTICE

**THIS DOCUMENT IS THE BEST
QUALITY AVAILABLE.**

**COPY FURNISHED CONTAINED
A SIGNIFICANT NUMBER OF
PAGES WHICH DO NOT
REPRODUCE LEGIBLY.**



GULF ELECTRONIC SYSTEMS

Gulf-EL-A12250

SEMIANNUAL TECHNICAL REPORT FOR THE PERIOD
JANUARY 1, 1972 TO JUNE 30, 1972

CARBON RESEARCH

Sponsored by
Advanced Research Projects Agency
Arlington, Virginia

ARPA Order No. 1861

August 25, 1972

R. J. Akins, J. L. Kaae, K. Koyama, R. J. Price, F. J. Schoen,
and J. C. Bokros (P.I.) (714-453-1000)

GULF OIL CORPORATION
GULF ENERGY & ENVIRONMENTAL SYSTEMS COMPANY
San Diego, California 92112

Program Code Number:	1D10	Contract Date:	June 26, 1971
Contract Amount:	\$226,235	Expiration Date:	June 25, 1973

This research was supported by the Advanced Research
Projects Agency of the Department of Defense under
Contract No. DAHC15-71-C-0282.

"The views and conclusions contained in this document
are those of the authors and should not be interpreted
as necessarily representing the official policies,
either expressed or implied, of the Advanced Research
Projects Agency or the U.S. Government."

GULF ELECTRONIC SYSTEMS
A DIVISION OF GULF ENERGY & ENVIRONMENTAL SYSTEMS COMPANY
P. O. BOX 608, SAN DIEGO, CALIFORNIA 92112

SUMMARY

Although the pyrolytic carbons deposited in fluid beds have structures and properties that can be varied over wide ranges, technological advances have been slow to develop. This is due to the lack of well-defined relations between the structure and properties of these carbons and to a poor understanding of the deposition process. The primary objective of this program is to provide the deposition-structure-property relations that are needed for expanded technological utilization.

During the first six months, several exploratory fields of structures were deposited using steady-state beds. Studies of these deposits revealed that the realization of the full-strength potential was not being achieved because of the presence of soot inclusions in the microstructure. Although improvements have been made by increasing the exit gas velocity and increasing the bed surface area, further improvement is desired. For this purpose, methane, a more stable hydrocarbon, is being used in the deposition.

X-ray data characterizing the carbon-silicon alloys that were deposited in the initial six-month period show that, contrary to the pure carbons, the crystallinity (the L_c parameter) of the silicon-alloyed carbons increases with increasing deposition temperature in the range 1150° to 1400°C. The trend toward larger L_c values with increasing propane concentrations is the same as for pure carbons, and is consistent with the suggested theory for carbon deposition in fluidized beds. Since carbon-silicon alloys with smaller L_c values are harder than alloys with larger values, stronger deposits are likely to be attained using higher propane and silicon concentrations and lower deposition temperatures.

A new injector system has been developed and tested which allows independent control of methyltrichlorosilane and hydrocarbon that can be metered into

the fluidized bed. This will expand the number of structures that can be deposited. In particular, this control will provide the means for depositing silicon-carbon alloys with both high silicon concentration and high carbon matrix density.

Thin sections, both parallel and perpendicular to the deposition plane, of pure and silicon-alloyed isotropic pyrolytic carbons were examined by transmission electron microscopy to observe the fine-scale structural features. A low-density carbon ($\rho = 1.55 \text{ g/cm}^3$) contained spherical growth features separated by pores. The spherical features, which are believed to originate with droplets of high-molecular-weight hydrocarbons during deposition, consisted of a relatively dense central nucleus surrounded by a less dense region containing crystallites whose form suggests tangled "tendrils." A high-density carbon ($\rho = 1.97 \text{ g/cm}^3$) also contained spherical structural features with central nuclei, but with edges that tended to be flattened and with smaller intervening pores. An isotropic carbon containing 8 wt-% silicon contained a uniform dispersion of $\sim 100\text{-}\text{\AA}$ particles of silicon carbide, whereas a sample containing 34 wt-% silicon had a heterogeneous structure in which spherical growth features free from silicon carbide alternated with regions containing a high density of silicon carbide platelets.

Strips of isotropic pyrolytic carbons deposited in steady-state fluidized beds were tested in three-point bending. The moduli of rupture were somewhat higher than those previously measured in four-point bending, particularly when a very small knife-edge spacing was used. However, the moduli of rupture were still significantly lower than for similar carbons deposited in non-steady-state beds. The modulus of rupture of a carbon deposited under conditions intended to minimize soot formation was not significantly different from that of carbon deposited under standard conditions.

A low-density and a medium-density carbon were fatigue-tested at 1800 cpm using cantilever beam specimens. With peak stresses greater than 90% of the mean single-cycle fracture stress, most samples survived 10^5 cycles without failure and some had not failed after 10^7 cycles. Thus, the endurance limit for these carbons is very close to the single-cycle fracture stress.

Wear data developed during the past six months indicate that under a fixed test situation, the wear rate varies with structure over two orders of magnitude. The wear resistance of low density (1.50 g/cm^3) isotropic pyrolytic carbon and that of glassy carbon (density = 1.50 g/cm^3) are similar and low. The highest wear resistance was exhibited by the silicon-alloyed pyrolytic carbons. Wear caused by pure titanium rubbing on carbon was catastrophic.

The in-plane thermal expansivity was measured for a series of isotropic pyrolytic carbons with densities ranging from 1.35 to 2.01 g/cm^3 . The expansivity increased linearly with the carbon density and reached a value of $6.4 \times 10^{-6} \text{ }^\circ\text{C}^{-1}$ (at 400°C) for a carbon with a density of 2.01 g/cm^3 .

Thermal conductivities of isotropic pyrolytic carbons are being obtained from the thermal diffusivities measured by the heat-pulse method. Recent literature values for the heat capacity of glassy carbon are being used to convert the thermal diffusivities to conductivities. Conductivities previously reported under this program are now believed to be in error due to the use of obsolete heat capacity data for massive, oriented pyrolytic carbon. The new values show the thermal conductivity of the carbons increasing with increasing measurement temperature up to $\sim 500^\circ\text{C}$. The thermal conductivity of the carbons correlates better with apparent crystallite size, L_c , than with the density. The conductivity increases with increasing L_c . Analysis of the thermal conductivity-versus-temperature curves indicates that the heat conduction path is tortuous and that the mean spacing of phonon-scattering crystallite boundaries is 100 to 300 Å.

The thermal conductivity of pyrolytic carbons containing 4 to 28 wt-% silicon is lower than that of pure carbon but shows a similar temperature dependence. The thermal conductivity of the alloyed carbons is evidently controlled by the carbon phase and may be affected by a small amount of substitutionally dissolved silicon.

SUMMARY

SUMMARY	iii
1. PROGRAM OBJECTIVES	1
2. DEPOSITION STUDIES	2
2.1. Introduction	2
2.2. Elimination of Soot Inclusions from the Deposits	3
2.3. Co-Deposition of Carbon and Silicon.	13
3. STRUCTURAL STUDIES	19
3.1. Details of Experimental Techniques	19
3.2. Structure of Low-Density Carbon.	20
3.3. High-Density Carbon.	25
3.4. Carbon Alloyed with Small Amounts of Silicon	25
3.5. Carbon Highly Alloyed with Silicon	31
4. MECHANICAL PROPERTIES.	35
4.1. Young's Modulus and Modulus of Rupture	35
4.2. Fatigue.	40
4.3. Wear	43
5. PHYSICAL PROPERTIES.	57
5.1. Thermal Expansivity of Pure Pyrolytic Carbons.	57
5.2. Thermal Conductivity of Pure Pyrolytic Carbons	61
5.3. Thermal Conductivity of Silicon-Alloyed Pyrolytic Carbons.	68
REFERENCES.	72
APPENDIX A: WORK STATEMENT	A-1

FIGURES

1. Microstructure of coating deposited from pure propane at 18 l/min total flow using helium gas as diluent. This coating was deposited in a standard-length coater tube (3.5 in. diam x 31 in. long)	8
---	---

FIGURES (Continued)

2. Microstructure of coating deposited from pure propane at 18 l/min total flow using argon gas as diluent. This coating was deposited using conditions identical to those of run 5638-9 except for the argon 9
3. Microstructure of coating deposited from pure propane at 18 l/min total flow using helium gas as diluent. This coating was deposited using a coater tube that had been shortened 39% (to 19 in.) to reduce the amount of condensed soot above the bed and allow a shorter path out of the coater 10
4. Microstructure of coating deposited from pure propane at 18 l/min total flow using helium gas as diluent. This coating was deposited using the same conditions as in run 5638-15 (short tube) but with the i.d. of the tube reduced from 3.5 in. to 2.0 in. 11
5. Microstructure of coating deposited from pure propane at 18 l/min total flow using helium gas as diluent. This coating was deposited using the same conditions as run 5638-15 but with larger surface area particles added during the run to reduce the supersaturation of carbon in the bed. 12
6. Plot of the L_c parameter as a function of bed temperature. 16
7. Microhardness versus silicon concentration for carbons co-deposited with silicon in the range 1200° to 1400°C from propane in helium with added CH_3SiCl_3 . The values in parentheses are the corresponding matrix carbon densities. Filled circles: $L_c = 32$ to 35 Å. Open circles: $L_c = 38$ 48 Å 18
8. Transmission electron micrograph of low-density isotropic carbon ($\rho = 1.55 \text{ g/cm}^3$); sample parallel to the deposition plane. 21
9. Transmission electron micrograph of low-density isotropic carbon ($\rho = 1.55 \text{ g/cm}^3$); sample perpendicular to the deposition plane 22
10. Transmission electron micrograph of low-density isotropic carbon ($\rho = 1.55 \text{ g/cm}^3$); sample parallel to the deposition plane. Dense nuclei can be seen in the centers of the round growth features. 23
11. Transmission electron micrograph of low-density isotropic carbon ($\rho = 1.55 \text{ g/cm}^3$); sample parallel to the deposition plane. Outer less dense region is shown 24
12. Transmission electron micrograph of high-density isotropic carbon ($\rho = 1.97 \text{ g/cm}^3$); sample parallel to the deposition plane. 26

FIGURES (Continued)

FIGURES (Continued)

24.	Weight loss as a function of time in vibratory polisher for various pyrolytic carbon deposits (abrasive CS-46)	53
25.	Volume wear rate in vibratory polisher as a function of deposition temperature for carbons of this study (abrasive CS-46)	54
26.	Volume wear rate in vibratory polisher as a function of disc hardness (DPH) for pure and silicon-alloyed carbons (abrasive CS-46)	55
27.	Dependence of volume wear rate on silicon concentration for alloyed carbons.	56
28.	Dependence of volume wear rate on carbon matrix density for alloyed carbons.	56
29.	Thermal expansivity of isotropic pyrolytic carbons as a function of carbon density	60
30.	Heat capacity of carbons and graphite as a function of temperature.	62
31.	Thermal conductivity of isotropic pyrolytic carbon (run 5408-25) as a function of temperature.	64
32.	Thermal conductivity at 100°C of isotropic pyrolytic carbons as a function of carbon density.	66
33.	Thermal conductivity at 100°C of isotropic pyrolytic carbons as a function of apparent crystallite height, L_c	66
34.	Thermal conductivity at 100°C of silicon-alloyed pyrolytic carbons as a function of L_c . The numbers beside the points represent the percentage by weight of silicon.	70

TABLES

1.	Calculated minimum diameter of soot particle that would be in equilibrium (not be elutriated) with gases leaving top of fluidized bed for propane concentration of 40%	5
2.	Coating conditions and results for unalloyed LTI carbons deposited in steady-state fluidized beds from propane to reduce soot inclusions in deposits	7
3.	Deposition conditions for co-deposited carbon-silicon alloys in steady state beds using propane and methyltrichlorosilane	14
4.	Structural data for co-deposited carbon-silicon deposits formed in steady-state fluidized beds using propane and methyltrichlorosilane.	15
5.	Mechanical properties of deposit 5408-7 measured in three- and four-point bending	39

TABLES (Continued)

6.	Mechanical properties of two carbons of similar densities with different levels of soot inclusions	39
7.	Deposits used in vibratory polisher wear study	52
8.	Deposition conditions and structural parameters of pyrolytic carbons used for measurement of thermal expansivity.	58
9.	Thermal expansivity of pyrolytic carbons	59
10.	Deposition conditions, structural parameters, and thermal conductivity of pyrolytic carbons.	65
11.	Deposition conditions, structural parameters, and thermal conductivity of silicon-alloyed pyrolytic carbons.	69

1. PROGRAM OBJECTIVES

This report presents the results obtained during the second six months of the initial contract period. The objective of the program is to investigate the basic carbon deposition process in steady-state fluidized beds in order to obtain a better understanding of how specific carbon structures are formed. The deposition process is being manipulated with catalysts, and the number of structures attainable is being increased through the addition of alloying elements. The structures of the deposited carbon are being related to the deposition conditions, and variations in properties are being interpreted in terms of structure.* The first semiannual report may be consulted for background material.⁽¹⁾

*The complete Work Statement is given in Appendix A.

2. DEPOSITION STUDIES

(R. J. Akins)

2.1. INTRODUCTION

During the initial six-month period, several preliminary sets of experiments were carried out in which carbons were deposited in steady-state fluidized beds. The structures of the carbons were characterized and their mechanical properties were measured. These evaluations suggested that the full strength potential was not being realized in the carbons deposited in steady-state beds because an increased number of soot particles were becoming incorporated into the deposits during deposition. The elimination of these soot inclusions has been a prime objective in the deposition studies that were undertaken in the second six-month period.

In addition to the problem described above, the full range of alloying control for silicon-alloyed carbons was being restricted due to the use of a gas-liquid contactor (bubbler) for introducing the methyltrichlorosilane into the fluidized bed. Since the helium diluent gas is used as the carrier for methyltrichlorosilane, when high hydrocarbon concentrations are used, the volume flow of helium through the contactor is correspondingly low, thus leading to low silicon concentrations in these deposits (see Fig. 28 of Ref. 1). Accordingly, it was necessary to design a new system for the injection of methyltrichlorosilane, which permits the independent control of the amount of additive injected into the deposition chamber.

Descriptions of the steady-state deposition process, the methods used to characterize the carbon deposits and the pyrolysis conditions, and the raw materials have been reported in the first semiannual report.⁽¹⁾

2.2. ELIMINATION OF SOOT INCLUSIONS FROM THE DEPOSITS

When the pyrolysis conditions are such that a great excess of carbon forms in the gas phase of the bed, soot particles may be generated at a high rate and incorporated into the deposits. Examples of these inclusions are visible in Figs. B-1 and B-25 in Ref. 1.

Although the soot particles, when initially formed in the bed, are small enough to be elutriated from the bed by the fluidizing gases, some of these small particles may be captured and incorporated with the depositing carbon. Again, at a later stage, these particles may become involved in the deposition process. This phenomenon occurs when the small soot particles generated in the beds are lifted above the bed by the flowing gases. Before they can all be exhausted, many may agglomerate into the larger particles, which, when the aggregates become large enough, fall back into the bed and become incorporated with the depositing carbon.

Some of the ways to reduce the number of soot inclusions that occur in the deposits are:

1. Adjust the process flow conditions and equipment so that the soot that forms in the apparatus is efficiently removed.
2. Reduce the supersaturation of the pyrolyzing gas to reduce the rate of soot formation.

Consider the first approach. In a first approximation, it is assumed that a soot particle behaves according to Stokes law so that

$$3 \pi \eta v d = \pi/6 d^3 (\rho - \rho') g \quad (1)$$

where η = viscosity,

v = terminal velocity of the particle,

d = particle diameter,

ρ = particle density, and

ρ' = gas density.

Since ρ' is negligible when compared to ρ , Eq. 1 can be modified to

$$d = 0.1354 (\eta v/\rho)^{1/2} \quad (\text{cgs units}) . \quad (2)$$

Using Eq. 2, the minimum particle size that would not be elutriated from the bed may be calculated for various gas viscosities for a given soot particle density. This was done for several gases using a particle density of 1.4 g/cm^3 ; the data are listed in Table 1.

The data in Table 1 show that quite large soot particles can be elutriated from the zone just above the bed. However, the design of the coater furnaces is such that the gas temperature cools to around 200°C at the top of the coater. This cooling causes a factor of 3 decrease in velocity and a factor of 2 decrease in viscosity so that at the top of the coater the gas stream can carry particles that are only about $70 \mu\text{m}$ in diameter at a total gas flow rate of 15 l/min . This means that the larger particles can be "trapped" in the vertical tube above the bed. These particles can grow and fall back into the bed or become attached to the tube wall. Occasionally a large piece of soot may be dislodged from the wall and reenter the bed, where it is partially or completely fragmented and coated with pyrolytic carbon. This interpretation is consistent with the fact that carbon-coated soot flakes are routinely found in the bed after coating.

A series of experiments was carried out to determine the effectiveness of the various methods of removing excess soot from the apparatus and thus decreasing the concentration of soot particles in the bed. The following changes in pyrolytic conditions were made to accomplish this:

1. The total flow was increased from 15 l/min to 18 l/min .
2. Argon was substituted for helium to increase the viscosity of the fluidizing gas. The associated increase in mass flow is also reported to improve fluidization.⁽²⁾

TABLE 1
CALCULATED MINIMUM DIAMETER OF SOOT PARTICLE THAT WOULD BE IN EQUILIBRIUM (NOT BE ELUTRIATED)
WITH GASES LEAVING TOP OF FLUIDIZED BED FOR PROPANE CONCENTRATION OF 40%

Input Gas Feed Rate (l/min)	Effluent Gas Type	Effluent Gas Viscosity (g/sec-cm) ^(a)	Tube Diam. (in.)	Effluent Gas Velocity (cm/sec)	Particle Diam Elutriated From Bed (cm)
15	He	585 x 10 ⁻⁶	3.5	61	0.0216
15	Ar	650 x 10 ⁻⁶	3.5	61	0.0228
15	H ₂	265 x 10 ⁻⁶	3.5	61	0.0145
15	He + H ₂ (b)	428 x 10 ⁻⁶	3.5	61	0.0185
18	He + H ₂ (b)	428 x 10 ⁻⁶	2.0	223	0.0316
18	He + H ₂ (b)	428 x 10 ⁻⁶	3.5	73	0.0203
30	He + H ₂ (b)	428 x 10 ⁻⁶	3.5	121	0.0261

(a) At 1200°C

(b) Assuming all propane in a 40% mixture decomposes to carbon and hydrogen gas

3. A 39% shorter furnace tube above the bed was instituted to reduce the length in which soot particles might aggregate and grow to the point where they fall back into the bed.
4. The internal diameter of the furnace tube above the bed was reduced to increase the gas velocity above the bed.

In addition, an experiment was carried out using a very large bed surface area. Increasing the bed area provides a larger "sink" for the carbon that is formed; it also reduces the saturation in the gas phase and thus reduces the rate of soot formation. ⁽³⁾

The experimental details are presented in Table 2. As yet, only metallographic evaluations are available. The microstructures of the deposits are shown in Figs. 1 through 5. The results are given below.

Argon versus Helium. The use of argon as a diluent gas does not offer any advantage over helium. The lower thermal conductivity of argon may be detrimental to temperature control at the gas inlet. The higher viscosity and mass flow did not seem to make any appreciable difference in the amount of soot present in the microstructure (compare Figs. 1 and 2).

Short Coater Tube. Reducing the length of the coater tube by 39% reduced the amount of soot inclusions. The carbon deposited was harder, which may indicate that less soot was present.

Short Coater with Reduced Internal Diameter. Reducing the inside diameter of the coater tube by a factor of 1.8 increased the velocity of the exit gas by a factor of about 3 and reduced the number of soot inclusions in the deposit even more than when a short coater was used alone. This effect can be judged by comparing the microstructures of Figs. 3 and 4.

TABLE 2
COATING CONDITIONS AND RESULTS FOR UNALLOYED LTI CARBONS DEPOSITED IN STEADY-STATE FLUIDIZED BEDS FROM PROpane
TO REDUCE SOOT INCLUSIONS IN DEPOSITS(a)

Run Objectives	Run No.	Inert Gas Type	Bed Surface Area (cm ²) Initial	Bed Temp (°C)(b) Added	Carbon Deposition Efficiency (%)	Average Coating Rate (μm/min)	Microhardness (DPH), 50-g Load
High overall flow	5638-9	Helium	2300	8300	1240	23.6	7.6
Repeat of 5638-9 with argon	5638-11	Argon	2300	8300	1240	26.8	7.1
Repeat of 5638-6 but with short coater tube	5638-15	Helium	2300	6300	1240	20.8	6.5
Repeat of 5638-9 but with reduced i.d. in short coater tube	5638-17	Helium	2300	8300	1240	22.1	7.9
Repeat of 5638-9 but with larger bed	5638-23	Helium	3000	42000	1240	23.4	3.7

(a) All runs were made with 40% propane, and with the gases being metered into the coater at 18 l/min at room temperature.

(b) Interpolated values from Fig. 3 of Ref. 1



M38184-1

300X

Run 5638-9: 18 l/min, 1240°C, 40% C₃H₈
Diluent gas: helium; 3.5-in.-diam x 31-in.-long tube
Initial bed size: 2300 cm²
Bed size added: 8300 cm²
Carbon deposition efficiency = 28.6%
Coating rate = 7.6 $\mu\text{m}/\text{min}$
Microhardness: 186 DPH (50-g load)

Fig. 1. Microstructure of coating deposited from pure propane at 18 l/min total flow using helium gas as diluent. This coating was deposited in a standard-length coater tube (3.5 in. diam x 31 in. long). The microstructure shows the presence of large amounts of soot inclusions.



M38185-1

300X

Run 5638-11: 18 l/min, 1240°C, 40% C₃H₈
Diluent gas: argon; 3.5-in.-diam x 31-in.-long tube
Initial bed size: 2300 cm²
Bed size added: 8300 cm²
Carbon deposition efficiency: 26.8%
Coating rate: 7.1 μm/min
Microhardness: 166 DPH (50-g load)

Fig. 2. Microstructure of coating deposited from pure propane at 18 l/min total flow using argon gas as diluent. This coating was deposited using conditions identical to those of run 5638-9 except for the argon. Comparison with Fig. 1 shows little if any reduction in the amount of soot inclusion.

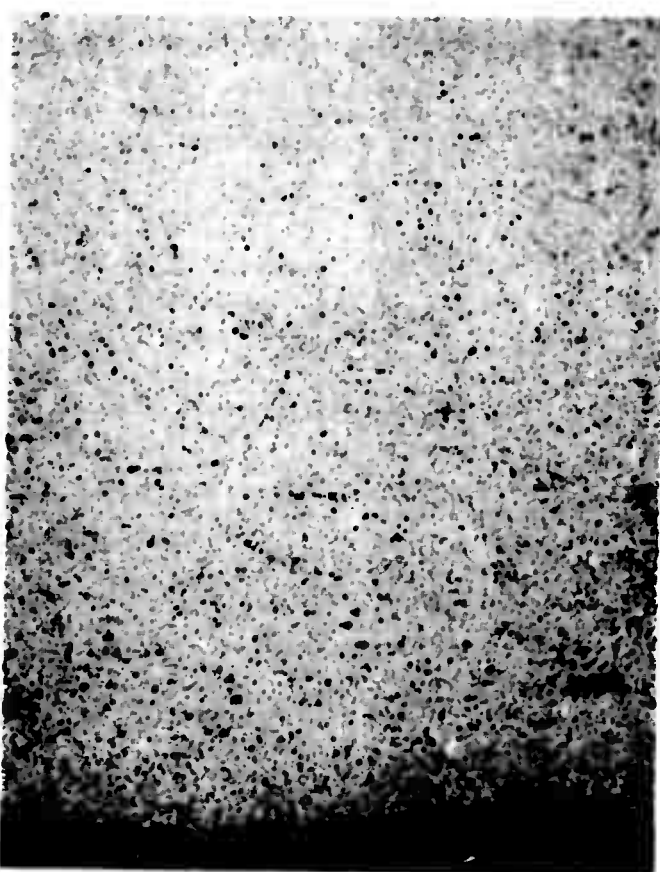


M38185-2

300X

Run 5638-15: 18 l/min, 1240°C, 40% C₃H₈
Diluent gas: helium; 3.5-in.-diam x 19-in.-long tube
Initial bed size: 2300 cm²
Bed size added: 8300 cm²
Carbon deposition efficiency: 20.8%
Coating rate: 6.5 μm/min
Microhardness: 226 DPH (50-g load)

Fig. 3. Microstructure of coating deposited from pure propane at 18 l/min total flow using helium gas as diluent. This coating was deposited using a coater tube that had been shortened 39% (to 19 in.) to reduce the amount of condensed soot above the bed and allow a shorter path out of the coater. The level of soot inclusions is slightly less than that shown in Figs. 1 and 2.

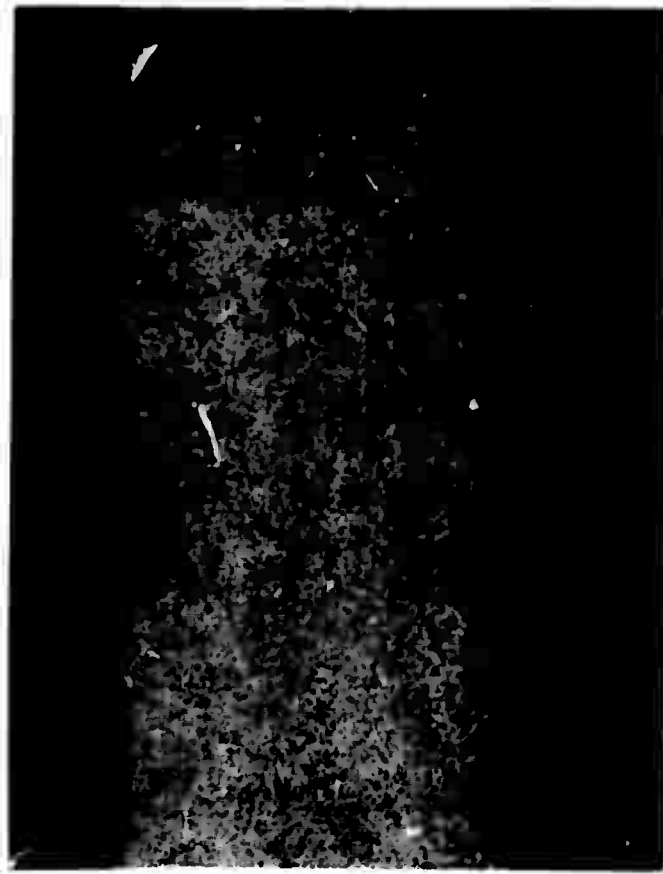


M38185-4

300X

Run 5638-17: 18 l/min, 1240°C, 40% C₃H₈
Diluent gas: helium; 2.0-in.-diam x 19-in.-long tube
Initial bed size: 2300 cm²
Bed size added: 8300 cm²
Carbon deposition efficiency: 22.1%
Coating rate: 7.9 μm/min
Microhardness: 213 DPH (50-g load)

Fig. 4. Microstructure of coating deposited from pure propane at 18 l/min total flow using helium gas as diluent. This coating was deposited using the same conditions as in run 5638-15 (short tube) but with the i.d. of the tube reduced from 3.5 in. to 2.0 in. The consequent higher velocity resulted in better soot elutriation. The microstructure contains fewer soot inclusions when compared to Fig. 3.



M38185-3

300X

Run 5638-23: 18 l/min, 1240°C, 40% C₃H₈
Diluent gas: helium; 3.5-in.-diam x 19-in.-long tube
Initial bed size: 3000 cm²
Bed size added: 42000 cm²
Carbon deposition efficiency: 28.4%
Coating rate: 3.7 μm/min
Microhardness: 196 DPH (50-g load)

Fig. 5. Microstructure of coating deposited from pure propane at 18 l/min total flow using helium gas as diluent. This coating was deposited using the same conditions as run 5638-15 but with larger surface area particles added during the run to reduce the supersaturation of carbon in the bed. The microstructure is very clean when compared to previous runs.

Short Coater with Large Bed. Increasing the surface area of the bed resulted in a very clean microstructure with a low level of soot inclusions. The microstructure obtained by increasing the surface area by a factor of 5 is depicted in Fig. 5.

Additional experiments, in progress, are needed to verify the effectiveness of the changes. Mechanical tests of the deposits shown in Figs. 1 through 5 are in progress. Another experiment is under way in which depositions from methane, a more stable hydrocarbon, are being used in an attempt to reduce the concentration and size of soot inclusions in the pyrolytic carbon that is deposited.

2.3. CO-DEPOSITION OF CARBON AND SILICON

Additional data further characterizing the silicon-alloyed carbons that were reported in the first semiannual report⁽¹⁾ have been obtained. The complete sets of data characterizing the deposition conditions and the structures of the deposited material are listed in Tables 3 and 4, respectively.

A plot relating the L_c parameter to the deposition temperature (Fig. 6) reveals a trend toward larger L_c values as the deposition temperature is increased. Comparison of these data with corresponding data for pure carbons (Fig. 12 of Ref. 1) indicates that there is a significant difference in the temperature dependence in the range 1150° to 1400°C. Contrary to the pure carbons, the silicon-alloyed deposits are more crystalline when they are deposited at higher temperatures.

It is worth noting that the trend toward larger L_c values with higher propane concentrations is the same for the pure carbons as it is for the silicon-alloyed deposits. This is consistent with the idea that the use of higher hydrocarbon concentrations for deposition at a given temperature near 1300°C favors more extensive polymerization in the gas phase and hence large graphitoid layers in the carbon that is formed.⁽³⁾

TABLE 3
DEPOSITION CONDITIONS FOR CO-DISPOSED CARBON-SILICON ALLOYS DEPOSITED IN STEADY-STATE
BEDS USING PROpane AND METHYLTRICHLOROSILANE(a)

	C_3H_8 Conc. (%)	Control Temp. (°C)	CH_3SiCl_3 Feed Rate (g/min)	CH_3SiCl_3 Volumetric Flow Rate (R.T.) (cm ³ /min)	Carbon Deposition Efficiency (%)	Silicon Deposition Efficiency (%)	Average Deposition Rate (μm/min)	Coating Thickness (in.)
5-08-07	7	1300	1290	3.7	1360	44.5	20.8	2.1
5-08-69	25	1300	1270	8.7	1360	55.4	36.7	3.6
5-08-65	50	1300	1235	5.9	950	42.5	44.7	5.5
5-08-61	7	1350	1340	7.2	1150	36.3	22.2	2.3
5-08-69	25	1350	1335	9.5	1520	65.2	43.2	4.8
5-08-77	50	1350	1295	6.0	960	54.5	67.6	5.9
5-08-85	7	1400	1390	9.2	1470	40.0	30.4	3.0
5-08-83	25	1400	1370	9.8	1560	55.0	29.8	6.8
5-08-67	60	1400	1350	5.0	800	58.4	36.1	5.9

(a) Total flow rate was 15 l/min (C_3H_8 and He) at room temperature.

TABLE 4
STRUCTURAL DATA FOR CO-DEPOSITED CARBON-SILICON DEPOSITS FORMED IN STEADY-STATE
FLUIDIZED BEDS USING PROPANE AND METHYLTRICHLOROSILANE(a)

Run No.	C ₃ H ₈ Conc. (%)	Control Temp (°C)	Bed Temp (°C)	Apparent Droplet Size (μm)	Silicon Content (wt-%)	Micro-hardness (DPH, 50-g Load)	Deposit Density (g/cm ³)	Calculated Carbon Matrix Density (g/cm ³)	SiC (vol-%)	Apparent Crystallite Height, L _c
5-57	7	1300	1290	0.14	23.0	430	2.178	1.88	22.5	35
5-59	25	1300	1270	0.20	15.0	352	2.105	1.92	14.2	35
5-55	60	1300	1235	0.22	8.0	295	2.064	1.97	7.4	32
5-51	7	1350	1340	(b)	28.0	397	2.158	1.77	27.2	38
5-59	25	1350	1335	0.15	16.0	212	2.062	1.87	14.9	40
5-57	60	1350	1295	(b)	9.5	201	2.085	1.98	8.8	39
5-55	7	1400	1390	0.10	34.0	378	2.149	1.64	32.9	38
5-53	25	1400	1370	(b)	13.5	279	2.063	1.92	12.6	48
5-57	60	1400	1350	(b)	4.0	179	2.031	1.98	3.7	48

(a) The Bacon anisotropy factor for all deposits was <1.1.

(b) In progress.

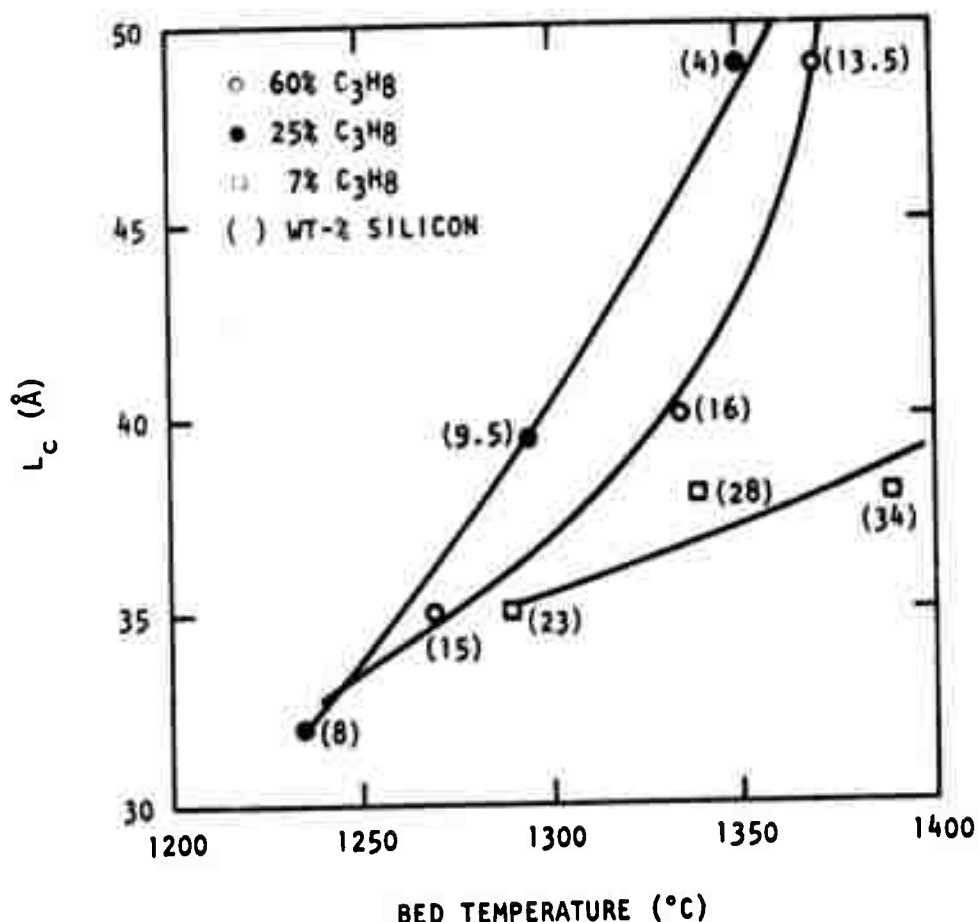


Fig. 6. Plot of the L_c parameter as a function of bed temperature

The variable responsible for the separation of hardness versus silicon concentration plots into two distinct sets of data (Fig. 29 of Ref. 1) is now identifiable. The plot (reproduced in Fig. 7 with added data) shows that the harder deposits (the upper curve) have L_c values in the range 32 to 35 Å, whereas the softer deposits (lower curve) have L_c values in the range 38 to 48 Å. The data in Figs. 6 and 7, together with those for pure carbons (Fig. 19 of Ref. 1), suggest that harder, stronger deposits are likely attainable by using high propane concentrations, low deposition temperatures, and higher silicon concentrations.

As pointed out in the introduction to this section, when a liquid-helium contactor is used to introduce the methyltrichlorosilane, it is not possible to attain high silicon concentrations in carbons deposited from high propane concentrations. Furthermore, since high carbon matrix densities are attained at high propane concentrations (see Fig. 27a in Ref. 1), the use of a liquid-gas contactor invariably leads to a deleterious decrease in the carbon matrix density when conditions are adjusted to obtain higher silicon concentrations in the deposit (see Fig. 28 in Ref. 1). Accordingly, a new injector system has been developed and tested which allows the independent control of the amount of methyltrichlorosilane that can be added to the deposition chamber. During the forthcoming contract period, the new system will be used to expand the field of structures attainable in the carbon-silicon system.

In addition, in an attempt to reduce the concentration of soot inclusions in the deposits, the use of methane as the hydrocarbon for co-deposition of carbon with silicon will be explored.

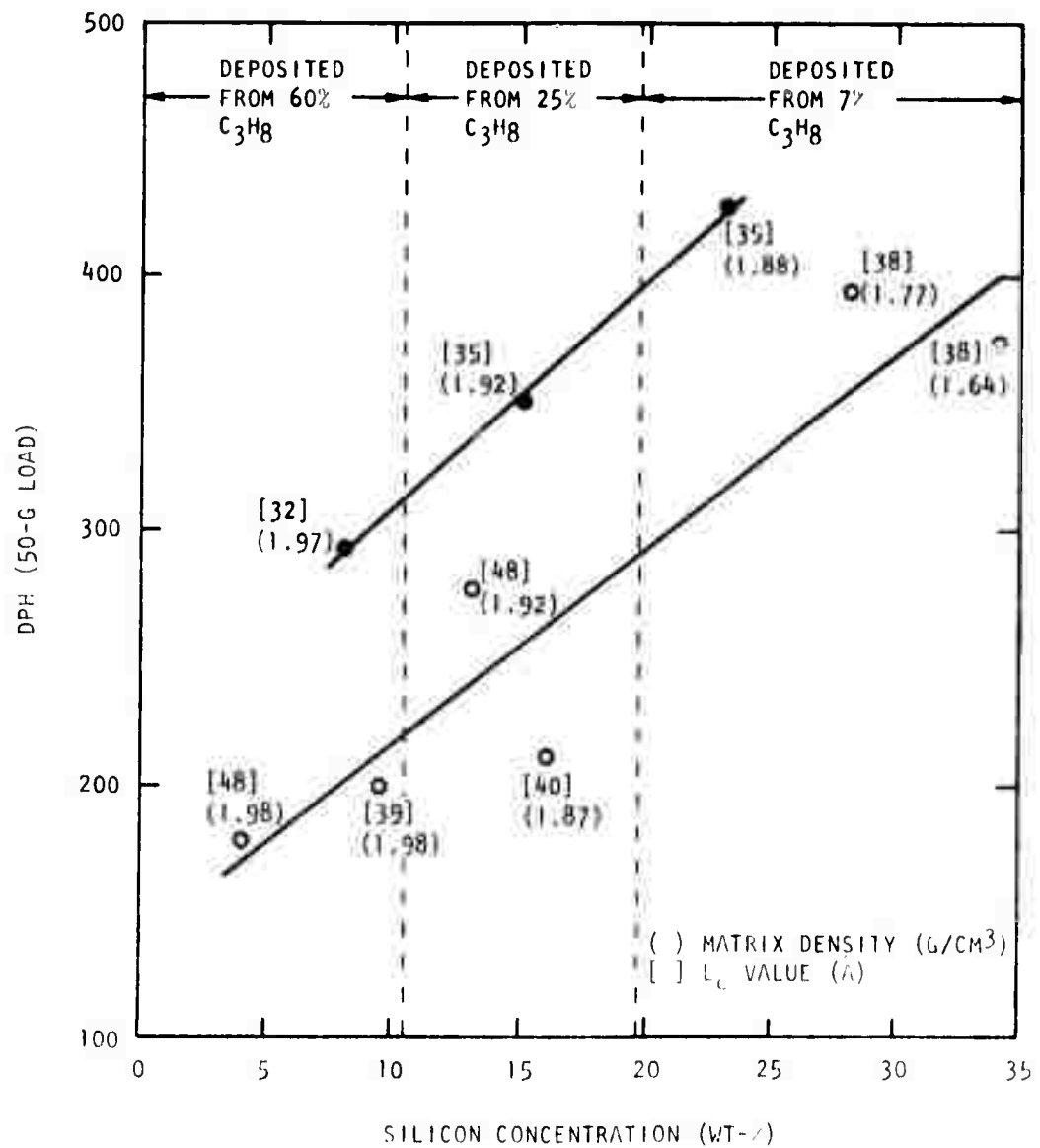


Fig. 7. Microhardness versus silicon concentration for carbons co-deposited with silicon in the range 1200° to 1400°C from propane in helium with added CH_3SiCl_3 . The values in parentheses are the corresponding matrix carbon densities. Filled circles: $L_c = 32$ to 35 \AA . Open circles: $L_c = 38$ to 48 \AA .

3. STRUCTURAL STUDIES (J. L. Kase)

There are subtle differences in the structure of glassy carbons and the isotropic pyrolytic carbons. These differences are responsible for the latter being substantially stronger and tougher.⁽⁴⁻⁶⁾ In an attempt to identify these differences and further characterize the isotropic pyrolytic carbons, their structures are being studied systematically using transmission electron microscopy.

Under the optical microscope, these isotropic carbons appear featureless. At higher magnifications using transmission electron microscopy, definite structural features and even atomic planes can be observed.

Observation of the microstructures of carbons by transmission electron microscopy has been hindered in the past by lack of a suitable thinning technique. Recent studies, described in Ref. 7, have shown that ion sputtering is an effective technique for thinning carbonaceous materials. Using this method, thin sections of pure and silicon-alloyed carbons deposited in the present program are being studied to reveal and characterize the structure on a submicron scale.

3.1. DETAILS OF EXPERIMENTAL TECHNIQUES

Deposits are being examined by transmission electron microscopy in two orientations: one allows observation parallel to the deposition plane; the other allows observation perpendicular to the deposition plane. The specimens used for observation perpendicular to the deposition plane were obtained by stripping the deposits from the graphite discs. The specimens used for observation parallel to the deposition plane were obtained by slicing wafers out of the coated graphite discs. Both types of specimens are mechanically ground and polished until they are about 0.001 in. thick and then polished

with 0.3- μ m alumina. The specimens can then be thinned in a sputtering device until perforation occurs. In the sputtering device the specimen is bombarded on both surfaces by a beam of argon ions, which strikes the surface at an angle of 10°. The apparatus is operated at an accelerating voltage of 6 kV and ion-beam current of 40 μ A. Preferential thinning at cracks and pores is not apparent, and large thin areas transparent to 100-kV electrons are consistently obtained.

The thinned specimens were examined in a Phillips EM 300 electron microscope.

3.2. STRUCTURE OF LOW-DENSITY CARBON

Transmission electron micrographs of a low-density isotropic carbon ($\rho = 1.55 \text{ g/cm}^3$) are shown in Figs. 8 through 11. The plane of the specimen shown in Fig. 8 is parallel to the deposition plane. Many circular features with pores between them are visible at the lowest magnification (Fig. 8). Since features that are circular when viewed perpendicular to the deposition plane are also circular in cross section (Fig. 9), they must be spherical in shape. These features are thought to be the remnants of droplets of high-weight carbon-hydrogen polymeric molecules formed in the gas-phase and subsequently deposited on the substrate. ⁽³⁾

In a carbon without soot inclusions, the pores between deposited droplets are probably the Griffith flaws. Since the pore size is controlled by the size of the growth features, small droplet sizes would likely lead to stronger deposits.

At the higher magnification (Fig. 10) the features appear to be non-uniform in structure. They contain a central dense circular region which is uniformly encompassed by an outer, less dense region. The central dense region may be a soot particle which acted as the nucleus for the original droplet. Soot particles collected at the coater outlet are similar in size and appearance to the central regions of the circular features.



Fig. 8. Transmission electron micrograph of low-density isotropic carbon ($\rho = 1.55 \text{ g/cm}^3$); sample parallel to the deposition plane



EM2348-2

20,000X

Fig. 9. Transmission electron micrograph of low-density isotropic carbon ($\rho = 1.55 \text{ g/cm}^3$); sample perpendicular to the deposition plane



000052

40,000X

Fig. 10. Transmission electron micrograph of low-density isotropic carbon ($\rho = 1.55 \text{ g/cm}^3$); sample parallel to the deposition plane. Dense nuclei can be seen in the centers of the round growth features.



Fig. 11. Transmission electron micrograph of low-density isotropic carbon ($\rho = 1.55 \text{ g/cm}^3$); sample parallel to the deposition plane. Outer less dense region is shown. Arrows indicate coherently diffracting crystalline regions which take the form of "tendrils."

The substructure of the outer, less dense region viewed at high magnification (Fig. 11) resembles a tangled structure. Each small tendril appears to be composed of a packet of carbon layer planes; several tendrils are indicated by the arrows in Fig. 11.

3.3. HIGH-DENSITY CARBON

Transmission electron micrographs of a high-density isotropic carbon (1.97 g/cm^3) are shown in Figs. 12, 13, and 14. At the low magnifications (Figs. 12 and 13), structural features and pores similar to those found in the low-density carbon are visible. There are differences, however. The sides of the circular features are flattened, and the appearance perpendicular to the deposition plane (Fig. 13) is not quite the same as that parallel to the deposition plane (Fig. 12). In the former, regions are present which may have been formed by direct condensation of planar molecules on the deposit itself rather than on the gas-borne droplets. These regions do not uniformly encompass the small round nucleating particles. Several of these regions are shown by arrows in Fig. 13. Well-defined regions made up of droplets are also marked by arrows. The flattening of the sides of the growth features has resulted in reduction of the sizes of the pores, but a few rather large pores are still present.

At high magnification (Fig. 14) the substructure of the growth features is more uniform than that of the low-density carbon. Round features similar to the particles at the center of droplet remnants in low-density carbons are present in the center of circular features visible in the high-density carbon. Some are marked by arrows in Figs. 13 and 14. The particles at the center of the circular features are probably soot particles which acted as nuclei for the formation of the original droplet in the gas phase.

3.4. CARBON ALLOYED WITH SMALL AMOUNTS OF SILICON

The structure of a carbon alloyed with 8 wt-% silicon is shown in Figs. 15 and 16. Using dark-field microscopy, it was found that the small particles (about $0.1 \mu\text{m}$ in diameter) that are uniformly distributed through



EM2314-1

20,000X

Fig. 12. Transmission electron micrograph of high-density isotropic carbon ($\rho = 1.97 \text{ g/cm}^3$); sample parallel to the deposition plane

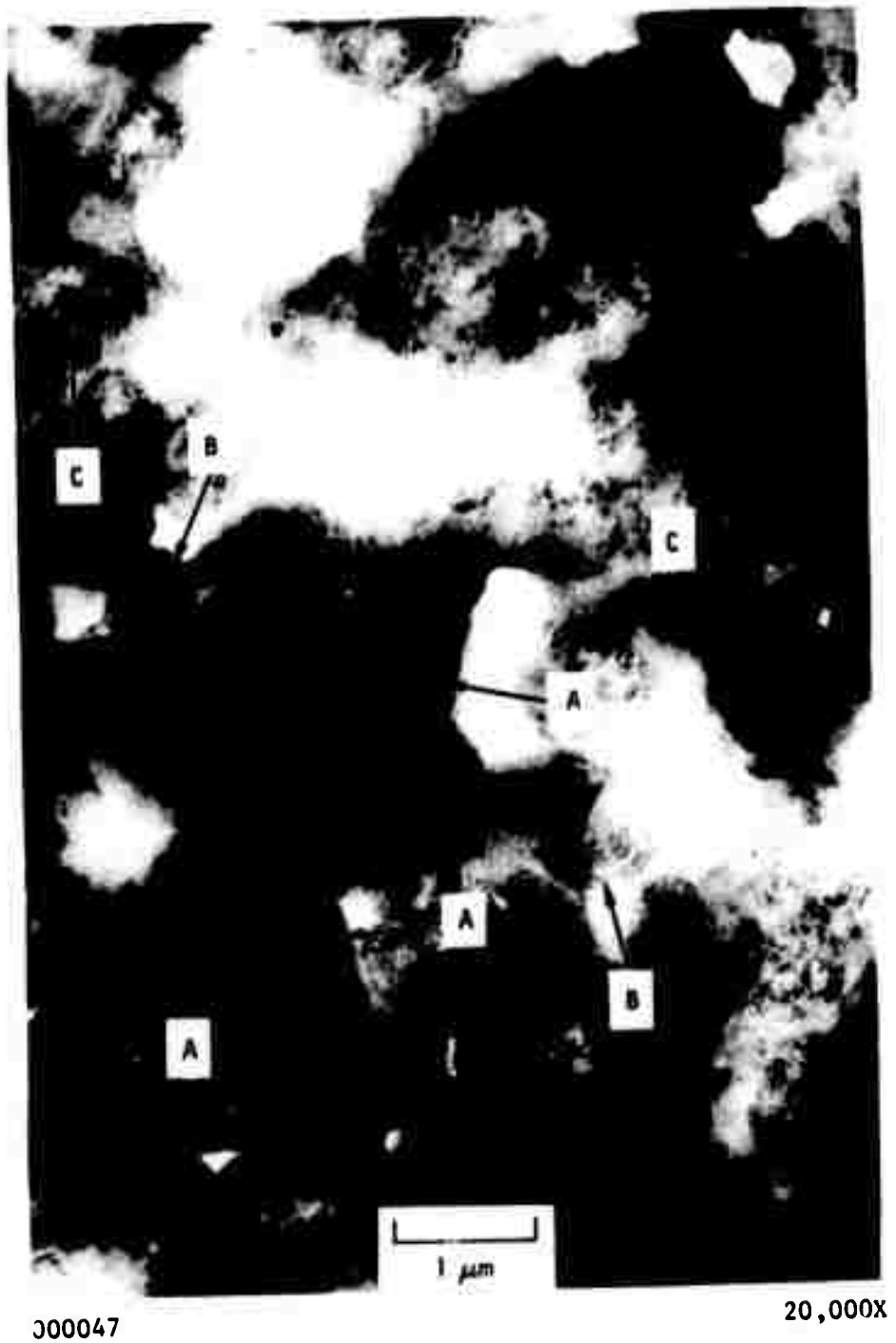


Fig. 13. Transmission electron micrograph of high-density isotropic carbon ($\rho = 1.97 \text{ g/cm}^3$); sample perpendicular to the deposition plane. A = region formed by direct condensation on the deposit; B = regions composed of droplets; C = round particles probably acting as nuclei.



EM2362-10

200,000X

Fig. 14. Transmission electron micrograph of high-density isotropic carbon ($\rho = 1.97 \text{ g/cm}^3$); sample parallel to the deposition plane. Arrow indicates round particles probably acting as nuclei.



000703

20,000X

Fig. 15. Transmission electron micrograph of isotropic pyrolytic carbon containing 8 wt-% silicon; sample perpendicular to the deposition plane



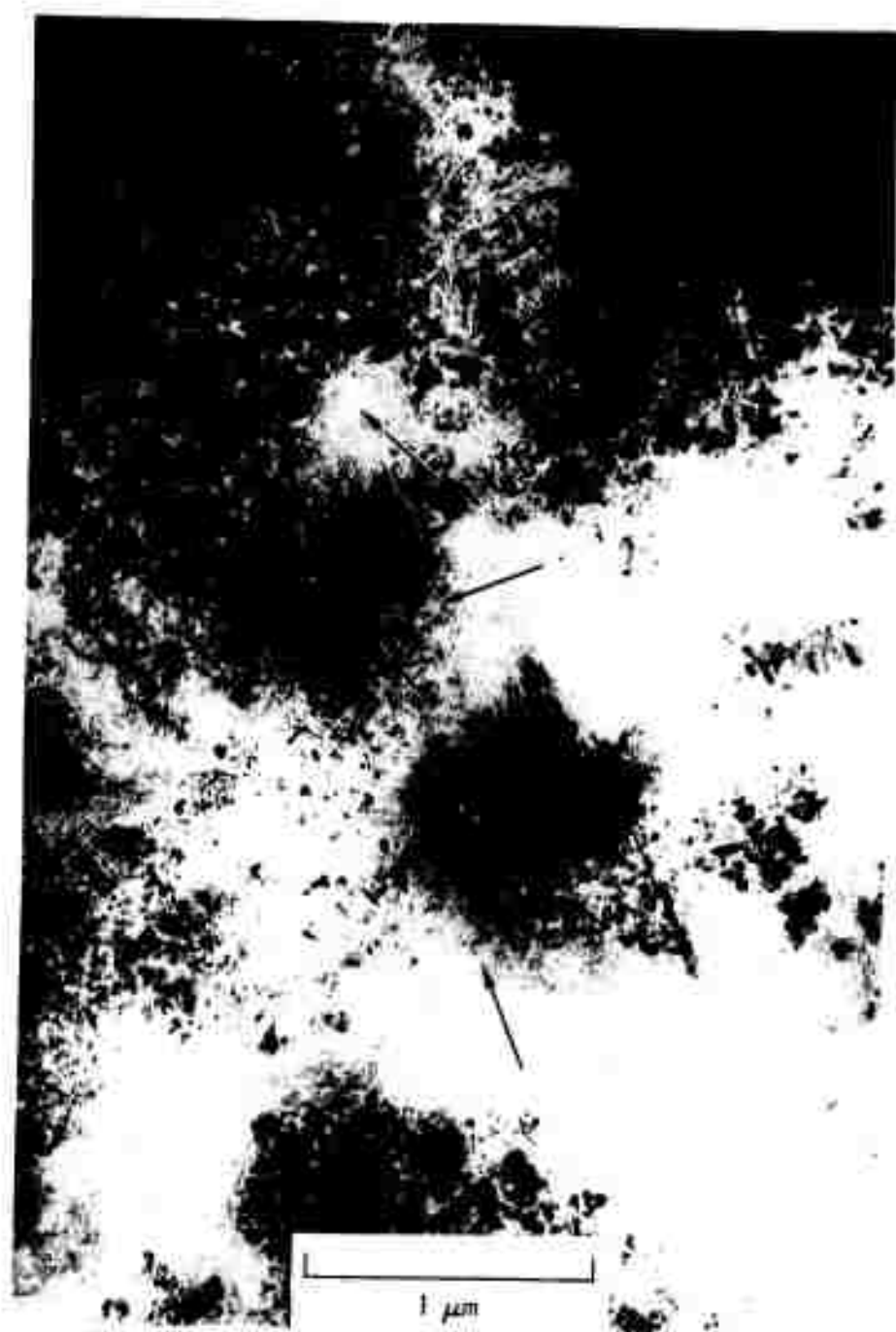
Fig. 16. Transmission electron micrograph of isotropic pyrolytic carbon containing 8 wt-% silicon; sample perpendicular to the deposition plane. Small dark particles are silicon carbide.

the microstructure are silicon carbide. Circular features and pores similar to those in the pure carbons are also visible. Since the silicon carbide is distributed throughout the circular features, the silicon carbide must be deposited at all stages of the deposition process. The silicon carbide is even present within and around the small nuclei of the circular features. This is considered to be evidence that the small silicon carbide particles are incorporated in the carbon in the gas phase as well as on the substrate during surface condensation.

3.5. CARBON HIGHLY ALLOYED WITH SILICON

The structure of a highly alloyed carbon (34 wt-% silicon) viewed perpendicular to the deposition plane is shown in Figs. 17 and 18. Circular features similar to the growth features in the pure carbons are marked by arrows on Fig. 17. No silicon carbide is visible in these features even at high magnifications. Other regions that were shown to be composed of a carbon matrix with many small single crystals of silicon carbide embedded in it are also evident. A high-magnification image of one of these regions (Fig. 18) shows irregularly shaped silicon carbide crystals containing many stacking faults (the sharp dark lines). Similar stacking faults have been observed in the grains of pure vapor-deposited silicon carbide.⁽⁸⁾ The more diffuse dark lines are probably extinction effects caused either by bending of the SiC crystals, by tilting of thin crystals with respect to the electron beam, or by thickness variations within thin crystals. Thus, in this highly alloyed carbon, the silicon carbide particles are much larger and their distribution is much more heterogeneous than in the carbon that contained 8 wt-% silicon.

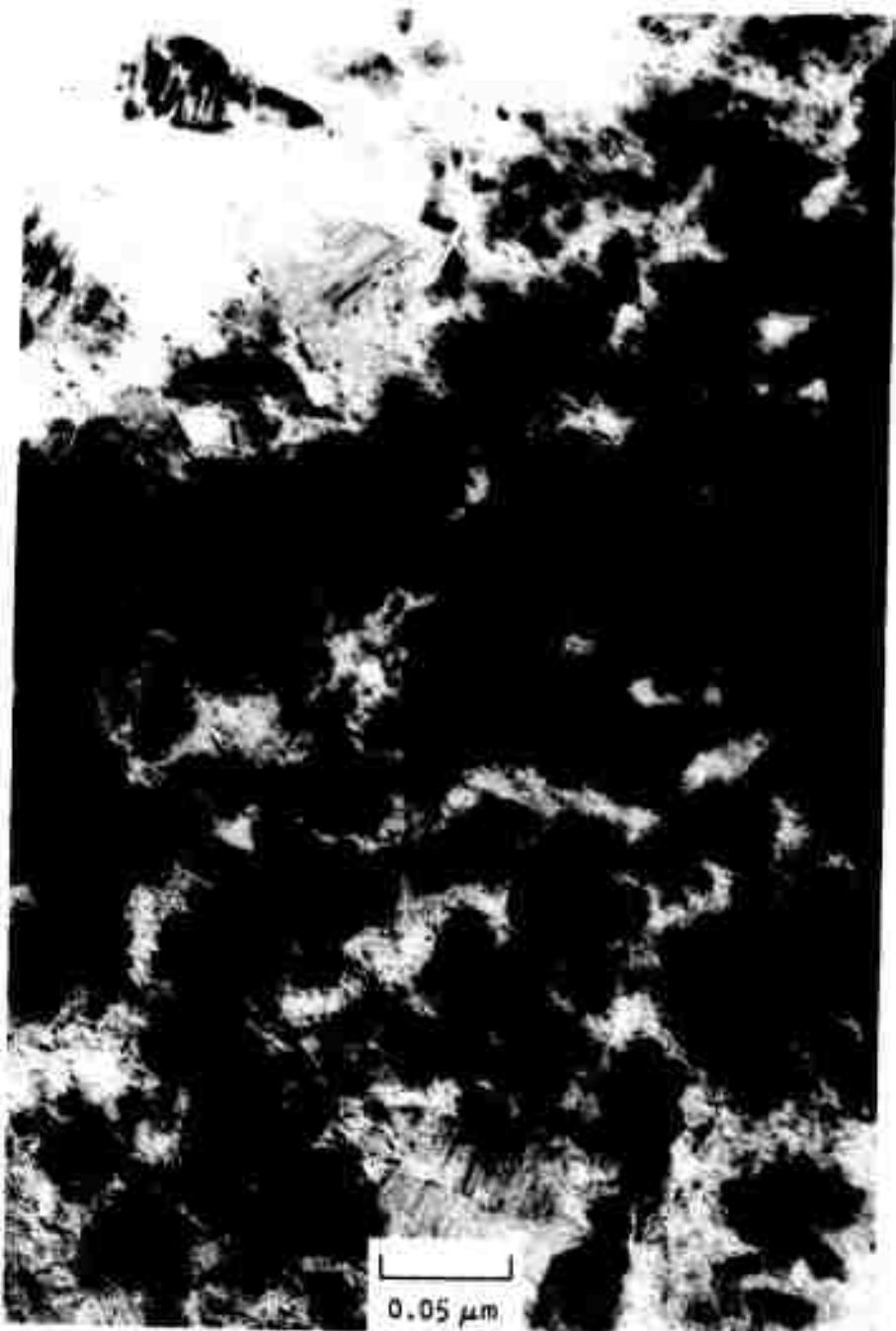
Comparison of the micrographs in this section with those for glassy carbons⁽⁹⁾ reveals a distinct difference in morphology. The glassy carbons appear to be made up of a tangle of long, spaghetti-like bundles of layer planes with no other organized substructure. The pyrolytic carbons, on the other hand, are made up of spherical features that are likely remnants of droplets that originated in the gas phase and were collected on the deposition surface in the fluid bed. Fractures in the isotropic pyrolytic carbon



000565

40,000X

Fig. 17. Transmission electron micrograph of isotropic pyrolytic carbon containing 34 wt-% silicon; sample perpendicular to the deposition plane. Arrows indicate circular growth features free from silicon carbide.



000572

350,000X

Fig. 18. Transmission electron micrograph of isotropic pyrolytic carbon containing 34 wt-% silicon; sample perpendicular to the deposition plane. Region contains many silicon carbide platelets.

propagate in a tortuous path between and around the droplet remnants, whereas fractures in glassy carbon propagate in an unhindered manner to form a conchoidal fracture surface.⁽⁶⁾ Hence, the toughness and strength of the isotropic pyrolytic carbons are likely a consequence of the inherently fine microstructure that originated in the initial deposition process.

4. MECHANICAL PROPERTIES

The mechanical properties of pyrolytic carbons are very structure-sensitive, and their control is important in developing useful load-bearing components. In the previous report, results of studies of the structure-property relations for the Young's modulus, the modulus of rupture, the fatigue strength, and the wear resistance were described. Further studies in these areas are described below.

4.1. YOUNG'S MODULUS AND MODULUS OF RUPTURE (J. L. Kaae)

In the previous report, the Young's modulus and moduli of rupture (measured in four-point bending) of the series of steady-state bed pyrolytic carbons were compared with the same properties of carbons deposited in non-steady-state beds (measured in three-point bending). It was found that the carbons deposited in steady-state beds had about the same Young's moduli as those deposited in non-steady-state beds providing they had the same density, but the moduli of rupture of the carbons deposited in steady-state beds were significantly lower. This difference was attributed to either or both of the following:

1. The two different testing techniques employed, i.e., four-point bending of larger specimens
2. The higher concentration of soot inclusions in the carbons deposited in steady-state beds.

To resolve this question, the properties of several of the carbons deposited in steady-state beds have been remeasured using three-point loading of small specimens. A few tests have been made on carbons deposited in steady-state beds using conditions designed to reduce the concentration of soot inclusions.

The four-point bending fixture that was used initially was described in the previous report.⁽¹⁾ The three-point bending fixture could be used with either of two outer knife-edge spacings, 0.2384 in. or 0.0775 in.; the first was nearly the same as was used to obtain the four-point bending results, and the second was the same as was used in earlier tests of smaller specimens of carbons deposited in non-steady-state beds. The specimen size was varied in each series of tests to assess the effects of specimen size.

The methods of specimen preparation were described in detail in Ref. 1. Briefly, disc-shaped specimens were stripped from the substrate discs, polished, and cut into 0.040-in.-wide strips using a diamond sectioning wheel. All specimens were examined for chips, scratches, and other defects under a microscope, and only defect-free specimens were tested.

Since the fracture stresses of the carbons are high compared with the Young's moduli, specimen deflections were large. Under these circumstances the usual small-deflection bending expressions, which assume small deflections and no frictional effects at the knife edges, do not apply. Accordingly, the three-point results were analyzed using expressions derived by Conway⁽¹⁰⁾ to calculate the Young's modulus and slope at the outer knife edges from the load and deflection at fracture, the specimen dimensions, and the loading configuration. Conway's expressions are:

$$\beta Y = \left[\cos(\phi_o - \alpha) \right]^{1/2} \left[F'(k) - F(k, \theta_1) - 2E(k) + 2E(k, \theta_1) \right]$$

$$- \left[2 \sin(\phi_o - \alpha) \right]^{1/2} \left[\sin(2\phi_o - \alpha) - \sin(\phi_o - \alpha) \right]^{1/2},$$

$$\beta \left[L + \tan(\phi_o - \alpha) Y \right] = \sqrt{2} \left[\sin \phi_o - \tan(\phi_o - \alpha) (1 - \cos \phi_o) \right]^{1/2},$$

where Y = deflection at center,

ϕ_o = slope of specimen at outer knife edges,

E = Young's modulus,

α = angle of friction for sliding over knife edges,

$$\beta = \left| P(1 - \mu^2)/EI \right|^{1/2},$$

$2P$ = load at center,

$2L$ = spacing of outer knife edges,

I = moment of inertia about neutral axis,

μ = Poisson's ratio,

$$\sin\theta_1 = \left[\frac{1 + \sin(\phi_o - \alpha)}{1 + \sin(2\phi_o - \alpha)} \right]^{1/2},$$

$$k = \left\{ 1/2 \left[1 + \sin(2\phi_o - \alpha) \right] \right\}^{1/2},$$

and $F(k)$, $E(k)$, $F(k, \theta_1)$, $E(k, \theta_1)$ are complete and incomplete elliptic integrals of the first and second kind.

Simultaneous solutions of the expressions may be obtained using Newton's method. The value of Poisson's ratio employed, 0.21, was that measured by Price and Kaae⁽¹¹⁾ for a poorly crystalline isotropic carbon with a density of 1.73 g/cm³. The friction angle determined by measuring the force required to pull a loaded specimen out of the testing fixture was found to be 7.2°. The maximum fiber stress at fracture, σ , was calculated from the expression

$$\sigma = [PL + PY \tan(\phi_o - \alpha)] h/2I$$

where h is the specimen thickness. The maximum fiber strain energy per unit volume at fracture, ϵ_f , was calculated from the expression

$$\epsilon_f = \sigma^2/2E$$

since the stress-strain curves were linear. The Young's modulus was calculated from the initial slope of the load-deflection curve using the small-deflection

bending expression. The method of analyzing the four-point results has been described in the previous progress report.⁽¹⁾

The results obtained by measuring the mechanical properties of a high-density carbon in three-point bending are listed in Table 5, along with the properties measured in four-point bending. The values are averages obtained by testing 12 specimens. The modulus of rupture increased when the testing method was changed from four-point bending to three-point bending with the same knife-edge spacing, and it increased again when a smaller knife-edge spacing was used. These increases are due to the decrease in the volume of the specimen subjected to the maximum stress. However, the fracture stress of the carbon deposited in a steady-state bed and measured in three-point bending is well below the 75-ksi modulus of rupture for the carbons deposited in non-steady-state beds, but measured in the same way. Therefore, it is concluded that the lower strength observed for the initial set of carbons deposited in steady-state beds is not due to the testing technique alone, but is due in part to structural differences between the carbons deposited in steady-state beds and those deposited in non-steady-state beds. The real differences in the moduli of rupture of the two carbons, however, are not as large as they first appeared.

In a second set of experiments, the mechanical properties of carbon deposited in a steady-state bed but using conditions designed to decrease the concentration of soot inclusions in the coating were measured. The microstructure of this carbon (5638-17) is depicted in Fig. 4. The results are given in Table 6, along with the properties of a carbon with similar density that was selected from the first series of coatings deposited in steady-state beds. The modulus of rupture of the "cleaner" coating is not significantly different. Apparently the attempt to reduce the number of inclusions in run 5638-17 was not effective. Efforts are being made to further clean up the microstructure.

TABLE 5
MECHANICAL PROPERTIES OF DEPOSIT 5408-7^(a) MEASURED
IN THREE- AND FOUR-POINT BENDING

Testing Technique	Outer Knife-Edge Spacing (in.)	Specimen Dimensions (in.)	Modulus of Rupture (ksi)		Young's Modulus (psi)	
			Av	Specimen Std. Dev.	Av	Specimen Std. Dev.
Four-point bending	0.297	0.040 x 0.010	45.5	7.2	3.59×10^6	0.05×10^6
Three-point bending	0.238	0.040 x 0.010	54.5	5.7	3.50×10^6	0.05×10^6
Three-point bending	0.077	0.040 x 0.003	59.2	5.8	3.81×10^6	0.10×10^6

(a) See Tables 2 and 3 of Ref. 1. This carbon had a density of 1.974 g/cm^3 , L_c of 36 \AA , and hardness of 219 DPH.

TABLE 6
MECHANICAL PROPERTIES OF TWO CARBONS OF SIMILAR DENSITIES
WITH DIFFERENT LEVELS OF SOOT INCLUSIONS

Run No.	Density (g/cm^3)	Modulus of Rupture (ksi)		Young's Modulus (ksi)	
		Av	Std. Dev.	Av	Std. Dev.
5408-21	1.91	47.1	5.1	3.58×10^6	0.05×10^6
5638-17	1.84	44.6	5.2	3.91×10^6	0.28×10^6

4.2. FATIGUE (F. J. Schoen)

The assessment of the possibility of failure of pyrolytic carbons under repeated application of load is important since most load-bearing applications involve cycle loading. There has been little work reported on the fatigue of carbonaceous materials, and none for pyrolytic carbons.

The details of the experimental techniques employed in fatigue tests were described in detail in Ref. 1. Briefly, specimens identical to those employed for measurement of the modulus of rupture and Young's modulus were used. The specimens were cyclically loaded in cantilever bending to a given deflection; the stress was calculated using Conway's expressions for three-point loading (see Section 4.1) since cantilever bending is the same as three-point with one-half the knife-edge spacing.

The results obtained to date for two carbons, a low-density carbon (5408-27) and a medium-density carbon (5408-5), are shown in Figs. 19 and 20. Even though stresses near the fracture stress were imposed on the specimens, many survived 10^5 cycles prior to failure. Some specimens did not fail at these stress levels, even after 10^7 cycles. It thus appears that the endurance limit of the low- and intermediate-density isotropic carbons is virtually identical to the single-cycle fracture stress. This is in contrast to the fatigue behavior of high-density graphites, whose endurance limits have been reported to correspond to a homologous stress of only 47%⁽¹²⁾ or 65%.⁽¹³⁾ It is worth noting that for AUF graphite at approximately 1950°C, Green⁽¹⁴⁾ has found an endurance limit equal to the single-cycle fracture stress. However, since mechanical behavior at elevated temperatures is quite different from that at room temperature, Green's result is likely not relevant.

The high endurance limit near the fracture stress of isotropic pyrolytic carbons might have been anticipated since mobile dislocations do not exist in these poorly crystalline materials.^(15,16) It is also consistent with a fracture mechanism described by a Griffith failure criterion. Such a mechanism for the isotropic pyrolytic carbons has been discussed.^(4,5) The

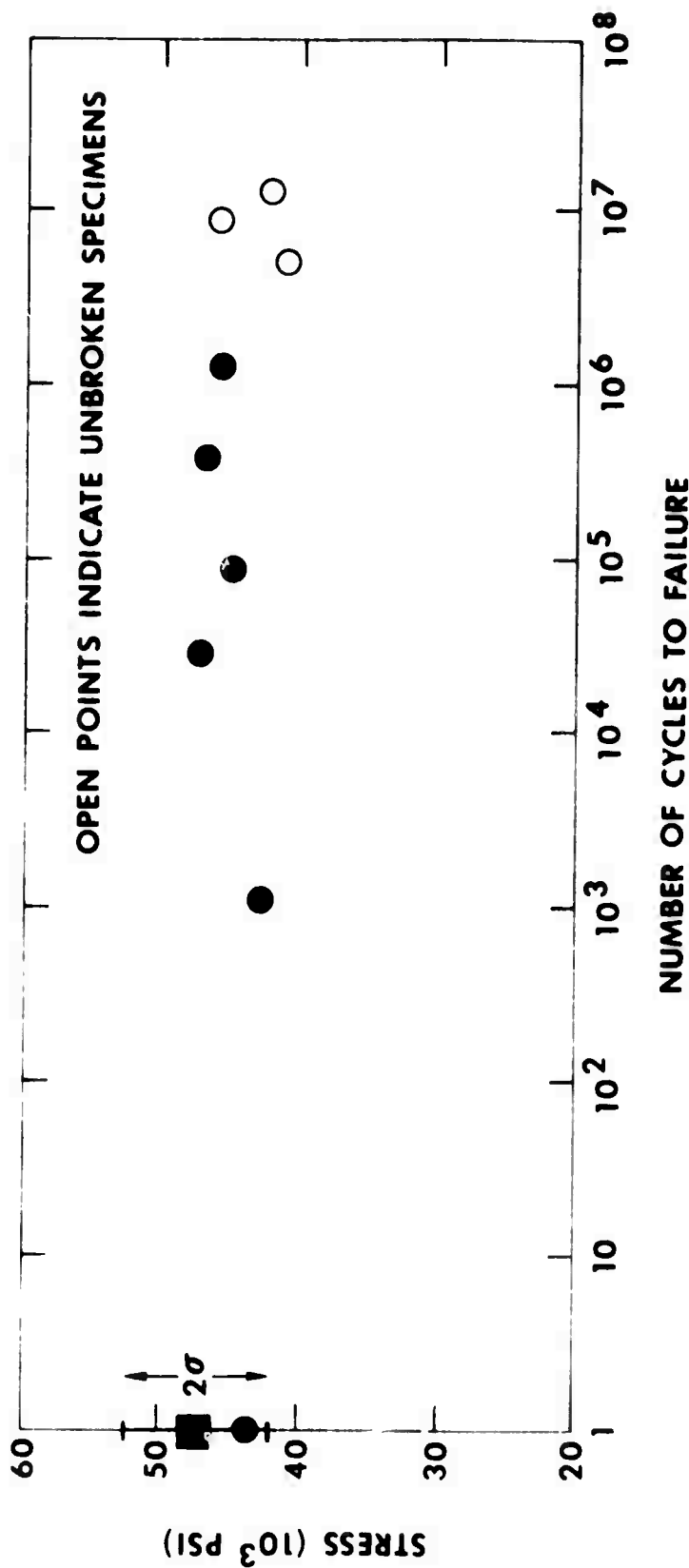
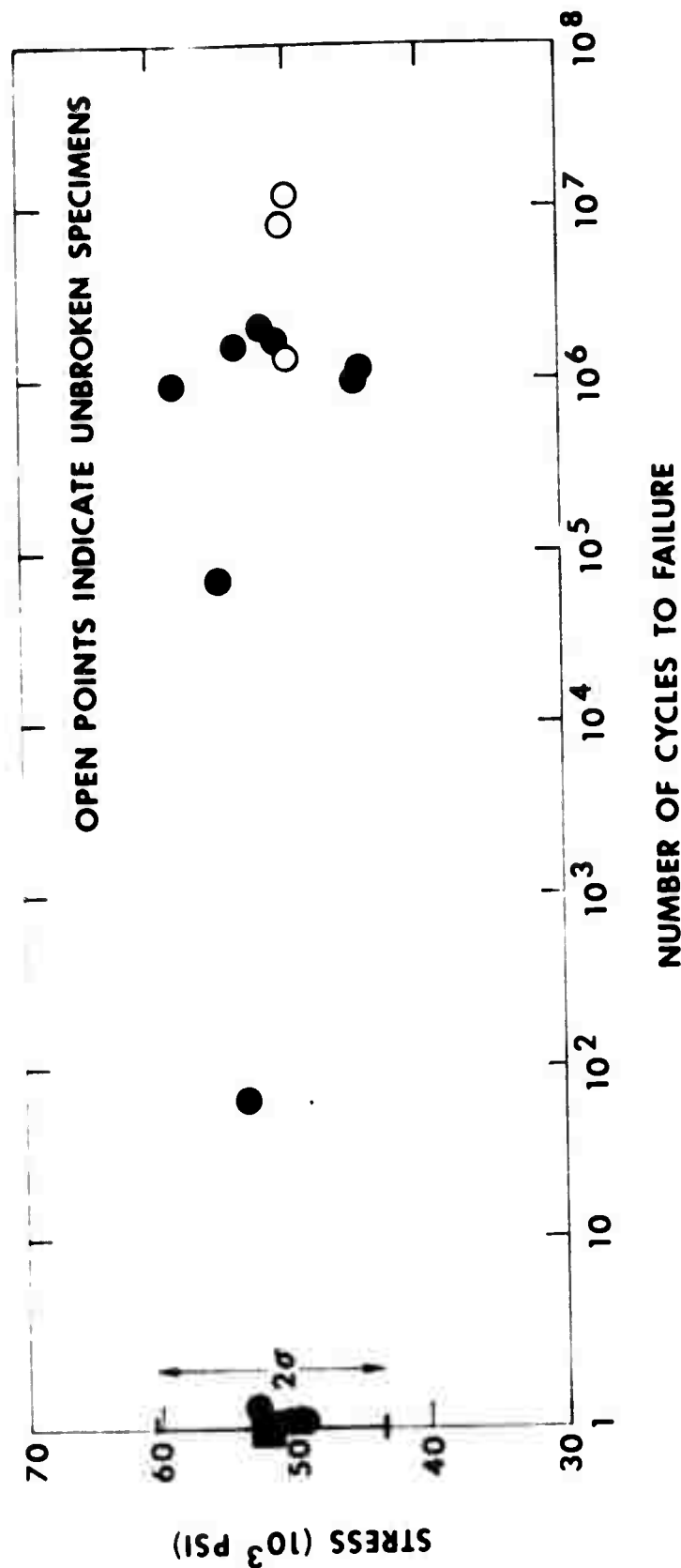


Fig. 19. Fatigue data for carbon of density 1.59 g/cm^3 . The single-cycle fracture stress is indicated by a filled square with its calculated standard deviations. The flexural Young's modulus of this deposit is $3.28 \times 10^6 \text{ psi}$. All data were obtained at 1800 cpm with a knife edge to specimen span of 0.223 in.



LC94061

Fig. 20. Fatigue data for carbon of density 1.78 g/cm^3 . The single-cycle fracture stress is indicated by a filled square with its calculated standard deviations. The flexural Young's modulus of this deposit is 4.05×10^6 psi. All data were obtained at 1800 cpm with a knife edge to specimen span of 0.223 in. (except for two tests in which 0.212 in. was used).

specimens that fractured after many cycles may have contained flaws that were initially subcritical but grew in a stable manner until they reached critical size and fracture occurred. If this interpretation is correct, many specimens must not have contained such flaws.

These studies are being extended to include the high-density and silicon-alloyed carbons.

4.3. WEAR (F. J. Schoen)

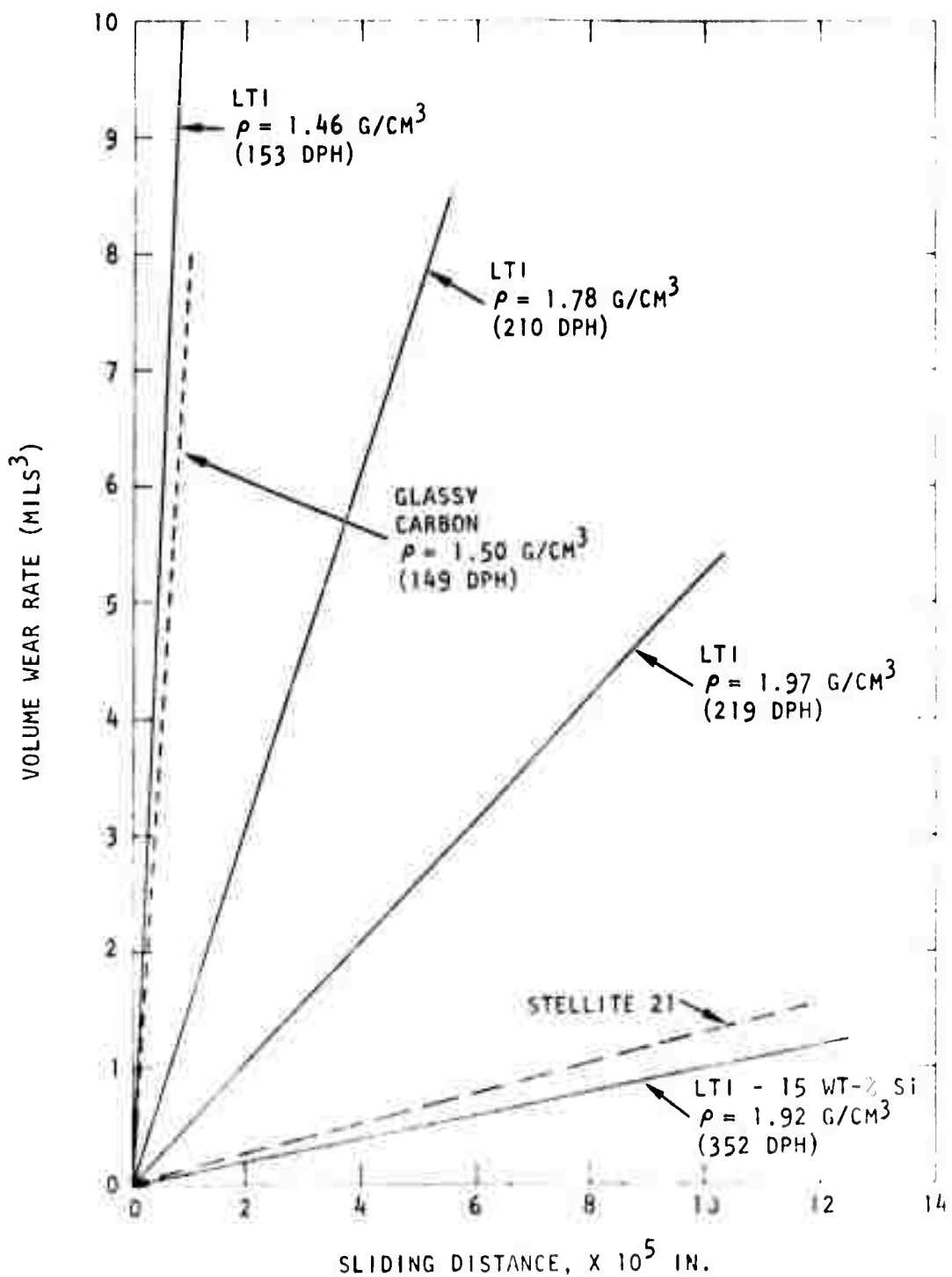
Although carbonaceous materials are used extensively as bearings and seals, little work has been reported on the wear properties of pyrolytic carbon, and there has been no work aimed at relating the wear properties of these materials to their structure.

The experimental methods used in this program and some basic dependences that have been found were reported in Ref. 1. The most fruitful method for relating wear properties to structure uses a system that permits the abrasion of a radiused, polished disc against a polished, flat plate. The load, sliding speed, environment, and materials used for the flat and disc are variables. The wear caused by the disc is measured on the plate.⁽¹⁾

It has been found that the wear on a given plate increases approximately as the 1/3 power of the load, and the volume of material removed from the plate by the abrading wheel increases linearly with sliding distance (see Figs. 39, 40, and 42 of Ref. 1).

During the past six months several new combinations of wear couples have been studied. Some couples included materials other than pyrolytic carbon. All the data presently available for pure carbon discs rubbing on various flats are plotted in Fig. 21. The data are for a load of 2.2 g and a disc speed of 60 rpm; the tests were conducted in water.

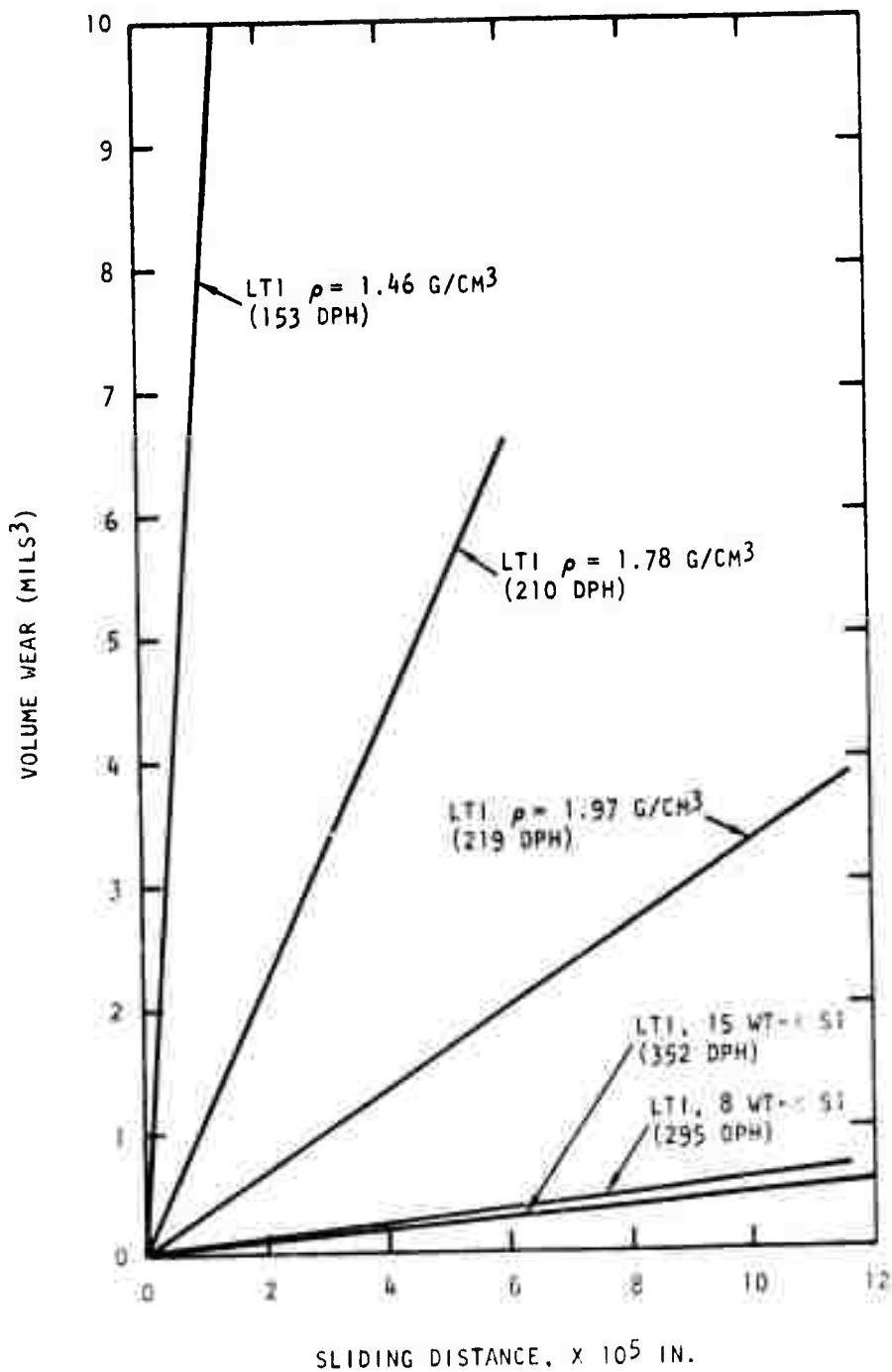
The data in Fig. 21a for a pure isotropic carbon disc with a density of 1.97 g/cm^3 demonstrate the magnitude of the variations that are possible



LC96090

(a)

Fig. 21. Wear caused by pure pyrolytic carbon discs rubbing on various flats. The load for all cases was 2.2 g. The disc speed was 60 rpm. All tests were carried out in distilled water: (a) for a pyrolytic carbon disc with a density of 1.97 g/cm³ and a hardness of 219 DPH.



LC96151

(b)

Fig. 21. Wear caused by pure pyrolytic carbon discs rubbing on various flats. The load for all cases was 2.2 g. The disc speed was 60 rpm. All tests were carried out in distilled water: (b) for pyrolytic carbon disc with a density of 1.78 g/cm^3 and a hardness of 210 DPH

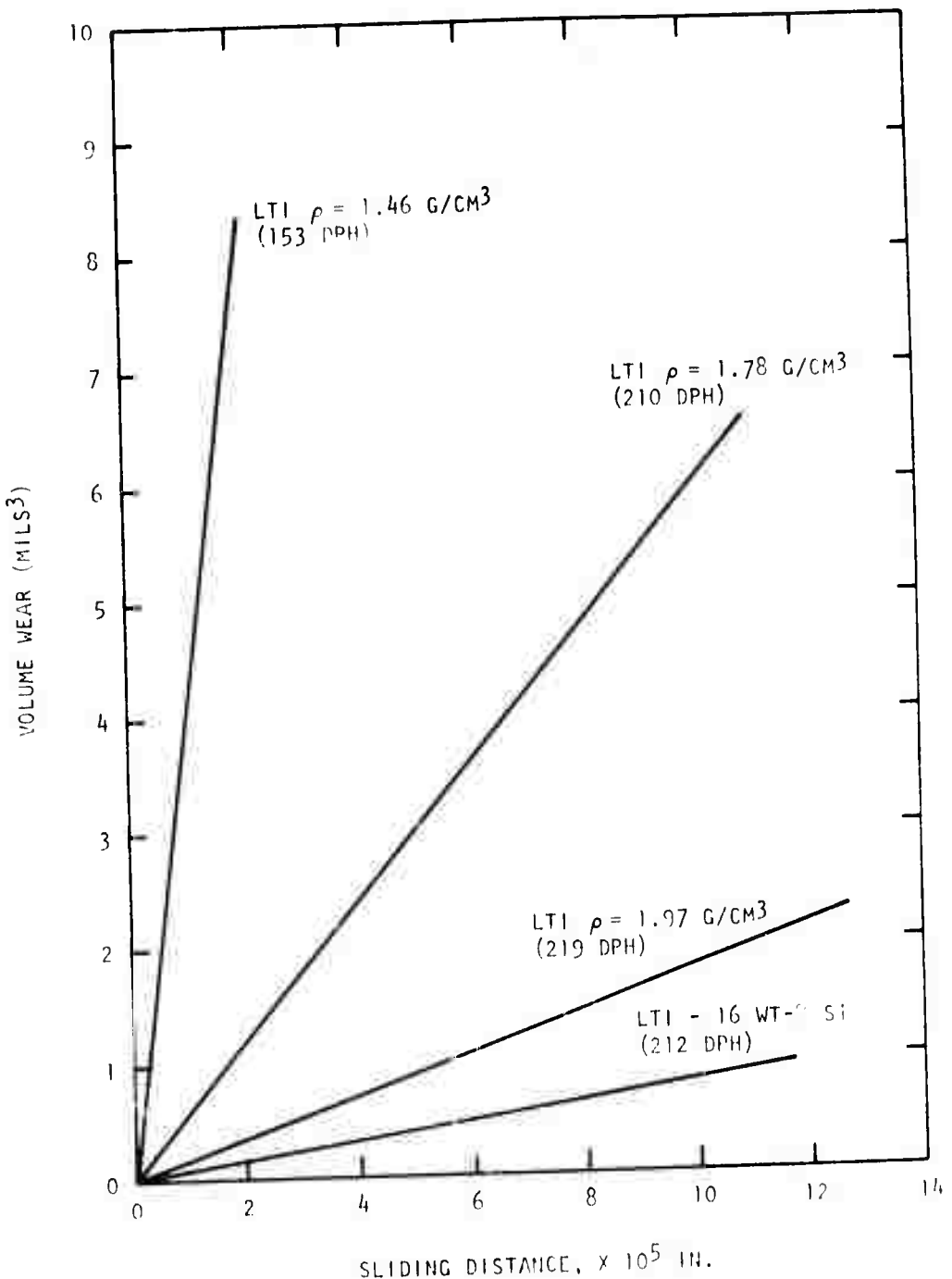


Fig. 21. Wear caused by pure pyrolytic carbon discs rubbing on various flats. The load for all cases was 2.2 g. The disc speed was 60 rpm. All tests were carried out in distilled water: (c) for pyrolytic carbon disc with a density of 1.46 g/cm^3 and a hardness of 153 DPH

as the structure of the flat is varied. The wear rates caused on the flats by the rotating disc are very high (~ 10 mils $^3/10^5$ in.) for both the low-density isotropic carbon and the glassy carbon flats. Increasing the density of the carbon flat from 1.46 g/cm^3 to 1.78 g/cm^3 reduces the wear rate by about an order of magnitude, increasing the density to 1.97 g/cm^3 decreases the rate further to $\sim 0.5 \text{ mils}^3/10^5$ in. Notice that the density and hardness of the flat increase concomitantly.

When Stellite 21 or silicon-alloyed carbon is used as the flat, the rate is very low ($< 0.2 \text{ mils}^3/10^5$ in.).

If the density of the disc is decreased, the wear rates on the flats are reduced (Figs. 21b and 21c). For example, when the density of the disc is reduced from 1.97 to 1.46 g/cm^3 , the wear rate on the pure pyrolytic carbon flat with a density of 1.97 g/cm^3 is reduced from $1.5 \text{ mils}^3/10^5$ in. to $0.18 \text{ mils}^3/10^5$ in. The wear rate for the silicon-alloyed carbon on Fig. 21c is less by more than a factor of 2 than that for the pure carbon with $\rho = 1.97 \text{ g/cm}^3$ even though their hardnesses are not significantly different. Since the carbon matrix density for the silicon-alloyed flat is 1.87 g/cm^3 , it may be concluded that the enhancement of the wear rate is due solely to the presence of SiC particles in the microstructure.

Plotted in Fig. 22 are the data for wear caused by different discs on a pure pyrolytic carbon flat with $\rho = 1.97 \text{ g/cm}^3$. The load, speed, and environment were the same as that used to generate the data in Fig. 21, i.e., 2.2 g, 60 rpm, and water, respectively. The relative rates for the pure carbons are what might have been expected, e.g., high for the high-density, hard-carbon disc and low for the low-density, softer carbon disc. The surprising results are the catastrophic wear caused by the titanium metal disc and the low wear caused by the relatively hard silicon-alloyed pyrolytic carbon disc.

The wear caused by the titanium disc on the carbon flat is two orders of magnitude higher than that caused by any other carbon disc. This may prove to be a consequence of chemical reaction between the titanium metal

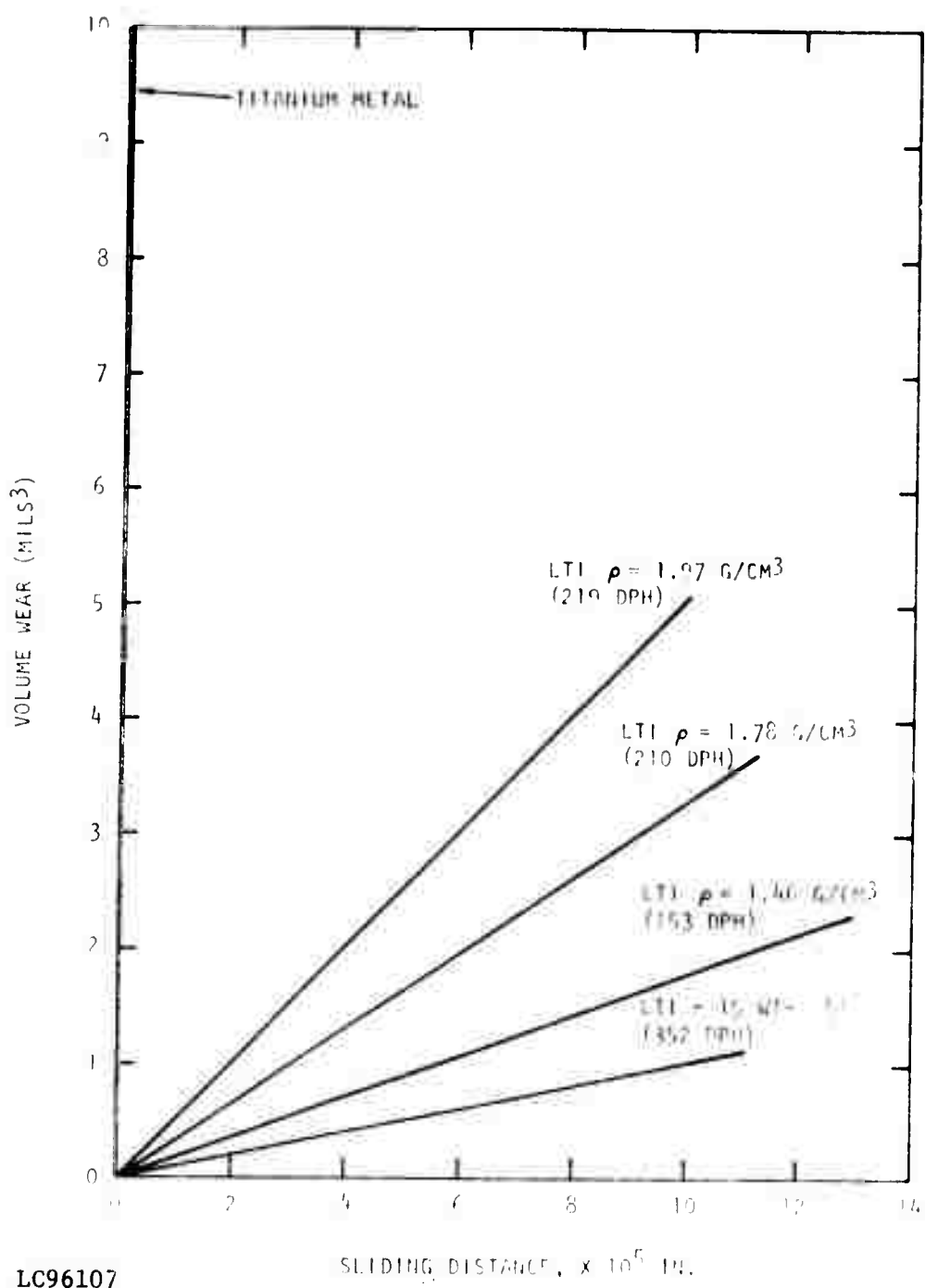


Fig. 22. Wear caused by various discs on an isotropic pyrolytic carbon flat. The flat had a density of 1.97 g/cm^3 . All tests were conducted in water using a load of 2.2 g and a disc speed of 60 rpm.

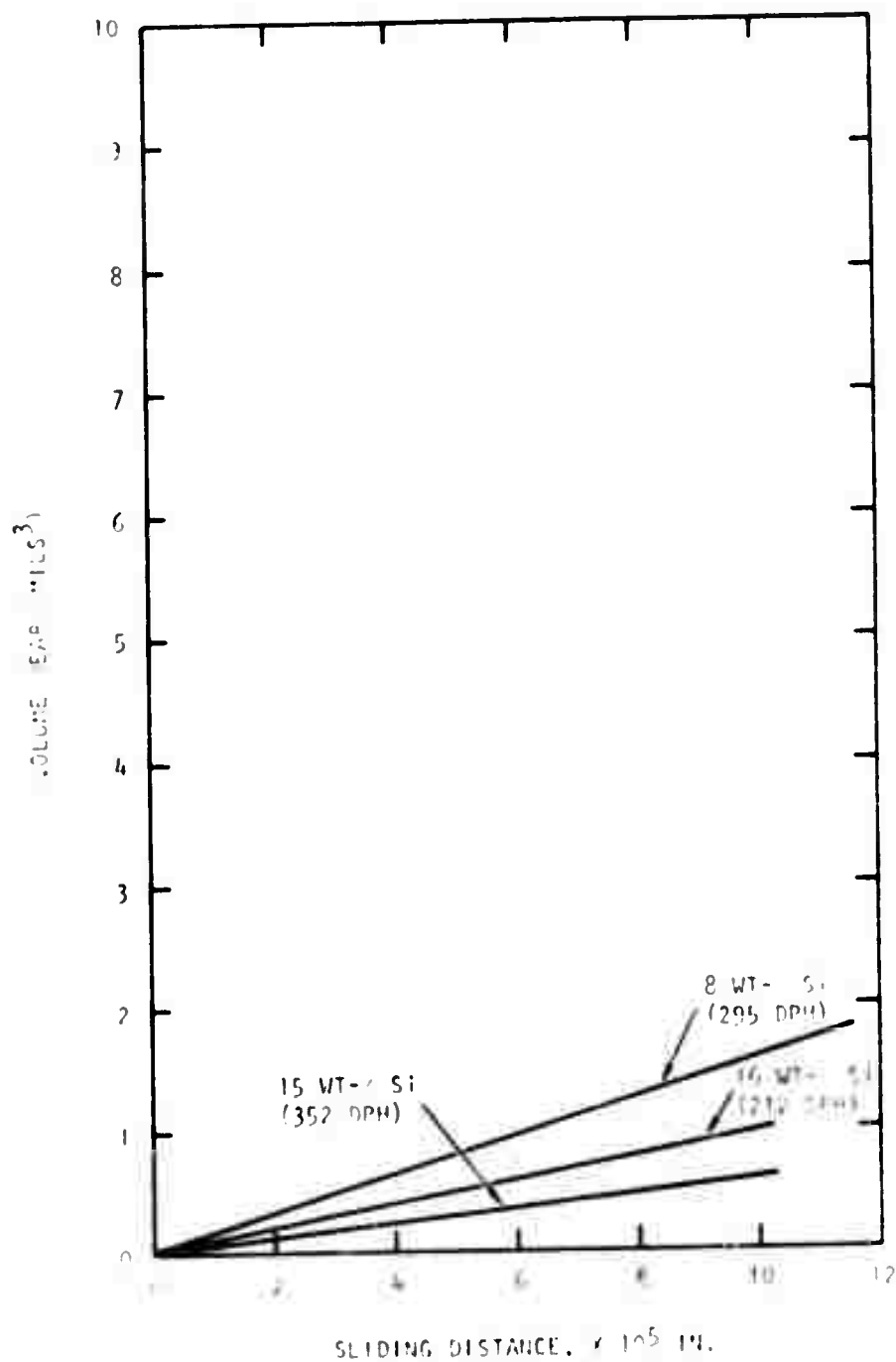
and the newly formed (and hence reactive) carbon surface. Analogous tests with Stellite 21 should yield interesting results, as should the wear caused by carbon discs on titanium flats.

One might expect the wear rate on the carbon flat in Fig. 22 to increase if the abrading disc were harder and contained SiC in the microstructure. The alloyed carbon disc has a carbon matrix density of 1.92 g/cm^3 and a hardness of 352 DPH, yet the wear caused by it is one-fifth that caused by a pure carbon disc with a density of 1.97 g/cm^3 and a hardness of 219 DPH. This means that the presence of silicon carbide in the microstructure decreases the wear on it caused by other carbon surfaces and reduces the wear caused by the alloyed material on other carbon surfaces. This result is of considerable technological interest.

The data that are available for wear caused by silicon-alloyed carbon discs rubbing on a silicon-alloyed flat are plotted in Fig. 23. The results indicate high wear resistance for silicon-alloyed carbon wear couples. The relative rates on Fig. 23 are not yet interpretable in terms of structural differences. Possibly the morphology of the SiC particles in the microstructure is the important variable. In any case, it is clear that the presence of SiC in the microstructure of either the disc or the flat greatly enhances the wear resistance.

In addition to the investigations of wear caused by the rotating disc-stationary flat situation, some exploratory studies were carried out using a vibratory wear test. The method is of interest because it provides a rapid and economical screening test for a large variety of carbons.

All tests were made on pyrolytic carbon coated graphite discs approximately 3/4 in. in diameter and 1/16 in. thick. The test device was a vibratory polisher (Model ST-1/2 Roto-Finish, Kalamazoo, Michigan) with an abrasive charge of $5/8 \times 5/16$ in. triangular chips of a SiC composition (CS-46, Fortune Industries, Chelsea, Michigan). Water was used as lubricant, with no additional polishing media. All the tests were carried out with the device intensity on the highest setting. Before the start of each test, the specimen discs were



LC96105

Fig. 23. Wear caused by various silicon-alloyed carbon discs rubbing on a silicon-alloyed carbon flat. All tests were carried out in water using a disc speed of 60 rpm and a load c. 2.2 g.

cleaned ultrasonically in ethanol or acetone and dried in a vacuum oven for at least 1/2 hr prior to weighing. Deposition conditions, structural data, and wear rates for the coating runs tested are given in Table 7.

Examples of weight loss versus time curves are given in Fig. 24. The wear was found to be linear with time; i.e., there is a constant wear rate. There is excellent agreement between tests on duplicate specimens. After an initial transient, there was no difference between the behavior of polished and as-deposited discs from the same coating run.

Figure 25 shows the volume wear rates (the slopes of curves plotted in Fig. 24 divided by the density) as a function of deposition temperature. The data fall on two separate curves, one for pure carbons and the other for materials alloyed with more than 10% silicon. Both sets of materials show a decreasing wear resistance as the temperature of deposition is increased, with no discernible trends according to concentration of hydrocarbon gas used in the fluidizing stream.

Volume wear rates were also correlated with the hardness of the disc (Fig. 26). As expected, for pure carbons, the wear resistance improves with increasing hardness of the disc specimen. The correlation holds for silicon concentrations up to about 15%. At higher silicon concentrations, the wear resistance decreases and the correlation with hardness disappears. The wear resistance may bear a relation to silicon concentration (Fig. 27), reaching a maximum wear resistance at 1^o to 20% silicon. A similar relation is obtained when carbon matrix density is used as the structural parameter (Fig. 28). The low wear resistance at higher silicon concentrations may be a result of the increased brittleness of the high silicon material or the wearing away of the carbon structure to form loose SiC particles that could act as an abrasive.

Although the vibratory method provides screening data rapidly and economically, the conditions of the tests are ill-defined; consequently, the correlations with structure are obscured. Accordingly, in future work the method will be used for screening tests only.

TABLE 7
DEPOSITS USED IN VIBRATORY POLISHER WEAR STUDY

Run No.	Load Temp (°C)	Conc. of C ₃ H ₈ Used in Deposition (%)	Hardness (DPH) (a)	Bulk Density (g/cm ³)	Carbon Density (g/cm ³)	Si (wt %)	Wear Rate (cm ³ /hr × 10 ³)
5408-23	1280	7	207	1.72	1.72	0	0.37, 0.78
5408-21	1190	25	226	1.92	0.59	0.59, 0.61	0
5408-11	1330	7	154	1.55	0	0.90	0
5408-5	1260	25	206	1.78	0	0.61, 0.61	0
5408-15	1260	25	190	1.76	0	0.68, 0.69	0
5408-3	1220	60	214	2.00	0	0.78, 1.01	0
5408-29	1400	7	100	1.35	0	2.15	0
5408-27	1340	25	156	1.59	0	1.02	0
5408-25	1300	60	170	1.75	0	0.74, 1.01	0
5408-33	1355	60	127	1.54	0	1.63	0
5408-35	1400	60	92	1.46	0	2.56	0
5408-87	1290	7	430	2.18	1.88	23	0.30, 0.56
5408-69	1270	25	352	2.11	1.92	15	0.26, 0.28
5408-65	1235	60	295	2.06	1.97	8	0.60, 0.56
5408-61	1340	7	397	2.16	1.77	28	0.57, 0.78
5408-59	1335	25	292	2.06	1.87	16	0.53
5408-57	1295	60	201	2.09	1.98	9.5	0.66
5408-85	1390	7	378	2.15	1.64	34	1.10
5408-83	1350	25	279	2.06	1.98	13.5	0.99
21C20(b)	--	--	306	--	--	11.5	0.56

(a) 50-g load

(b) A heart valve material

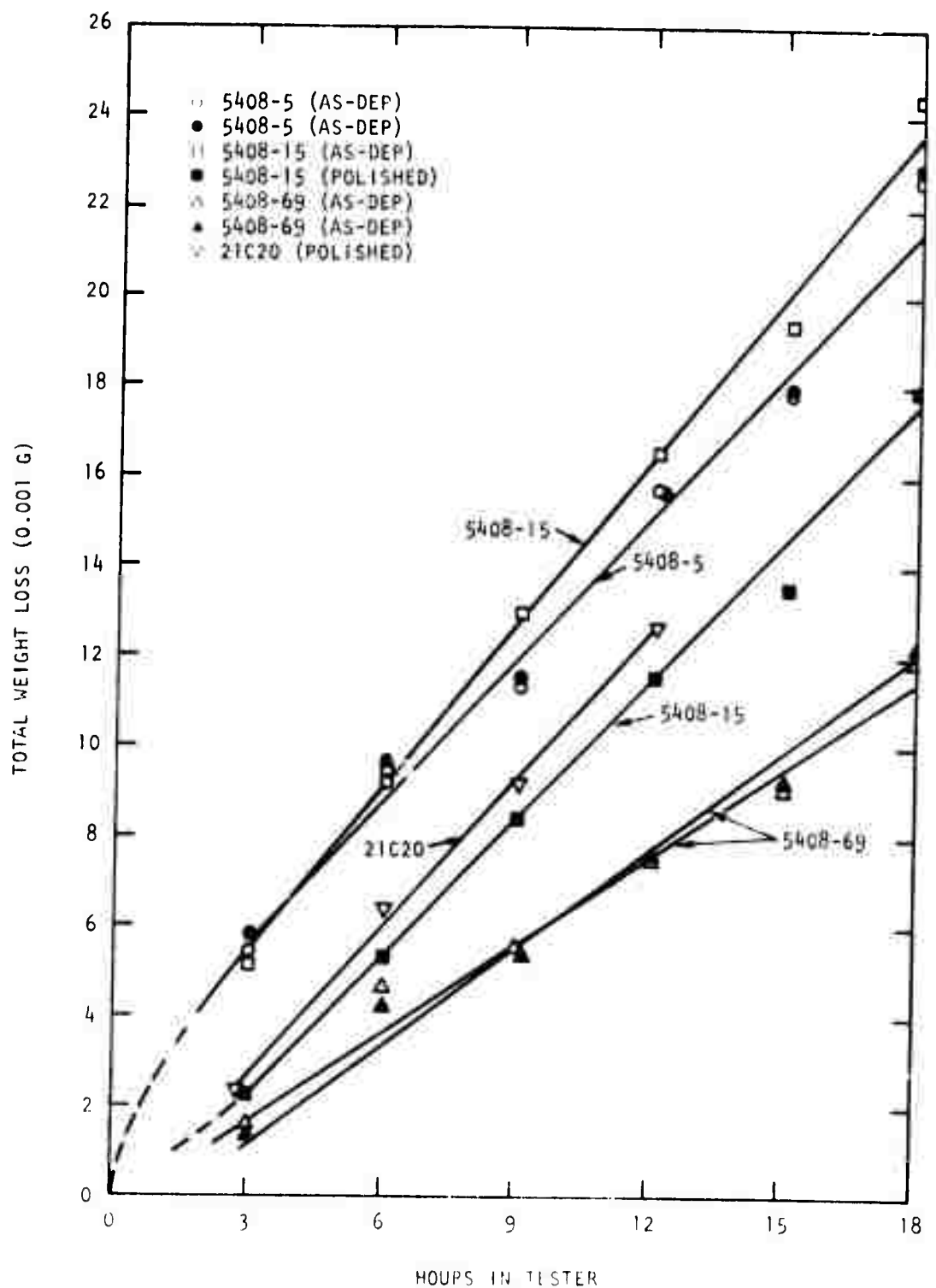


Fig. 24. Weight loss as a function of time in vibratory polisher for various pyrolytic carbon deposits (abrasive CS-46)

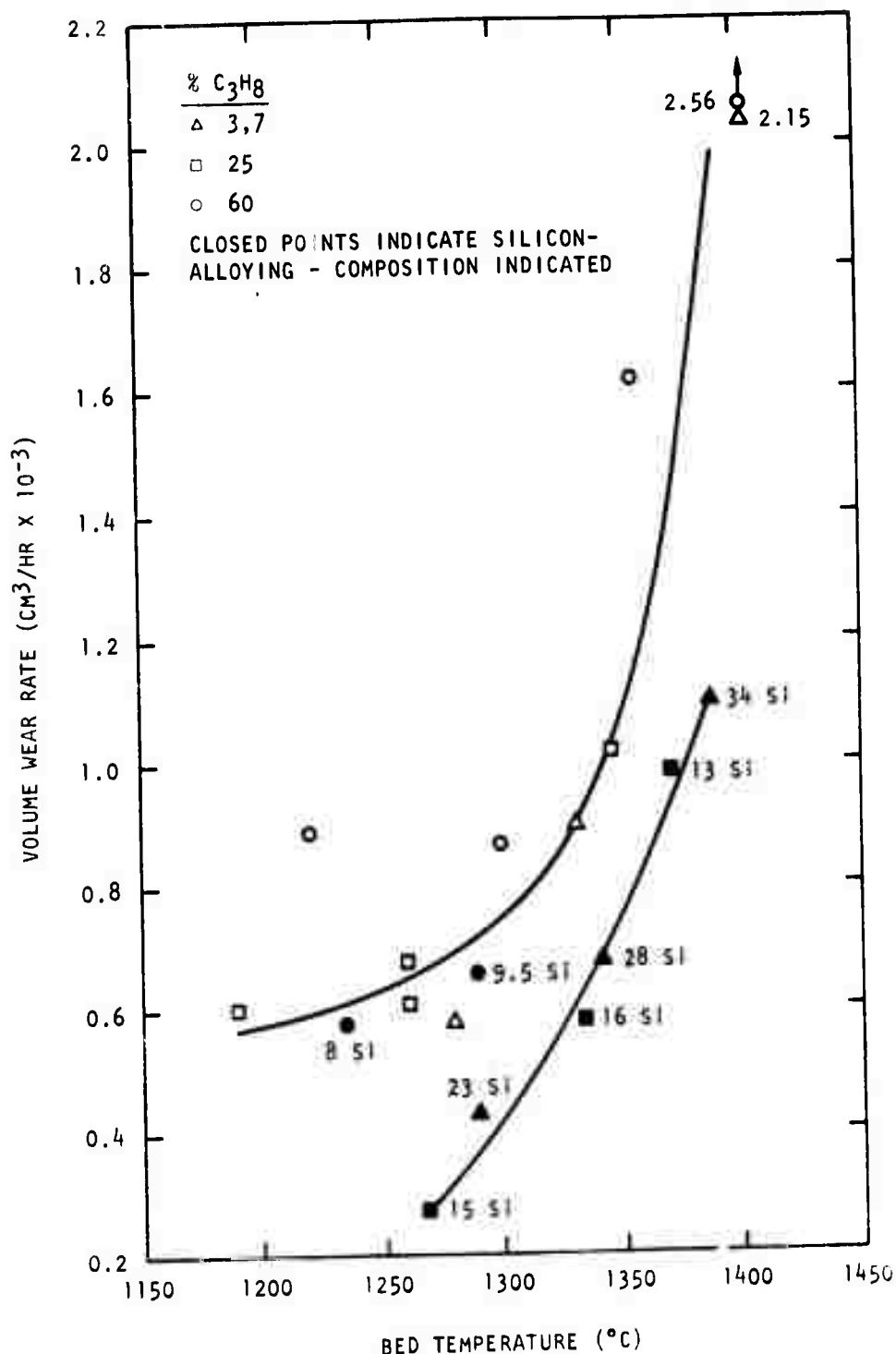


Fig. 25. Volume wear rate in vibratory polisher as a function of deposition temperature for carbons of this study (abrasive CS-46)

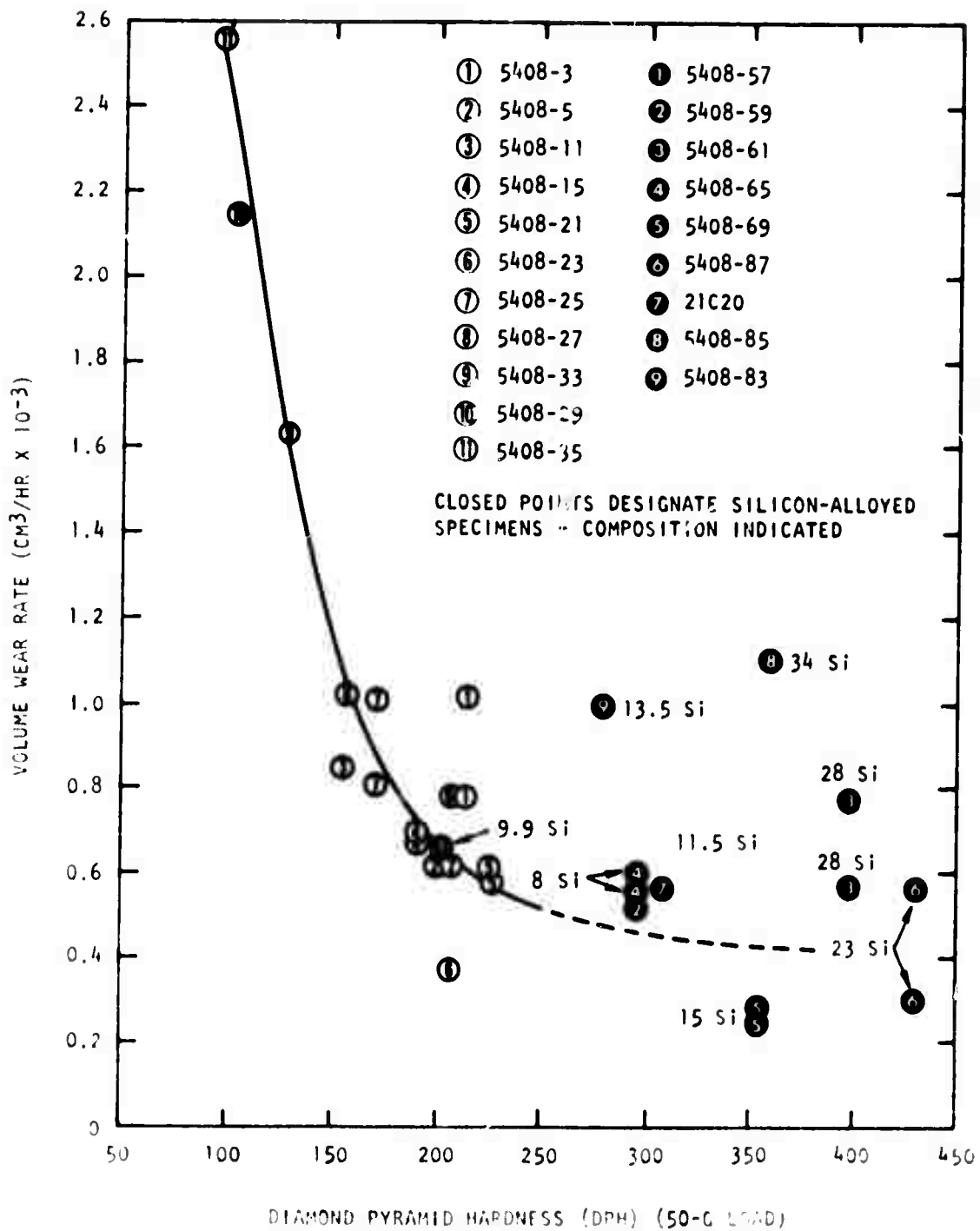


Fig. 26. Volume wear rate in vibratory polisher as a function of disc hardness (DPH) for pure and silicon-alloyed carbons (abrasive CS-46)

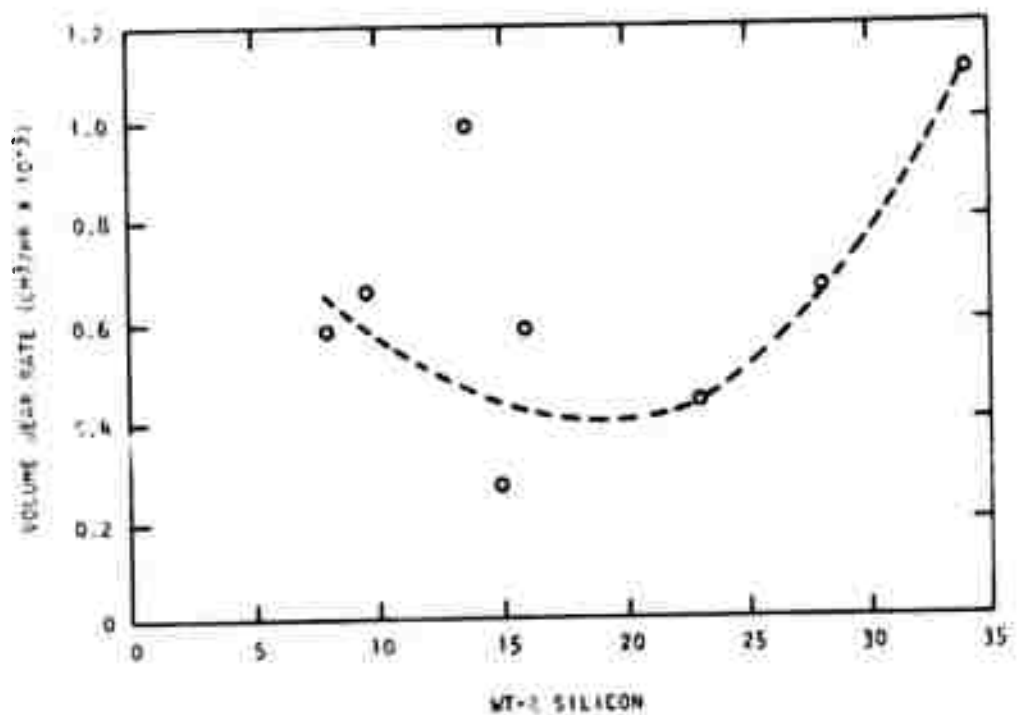


Fig. 27. Dependence of volume wear rate on silicon concentration for alloyed carbons

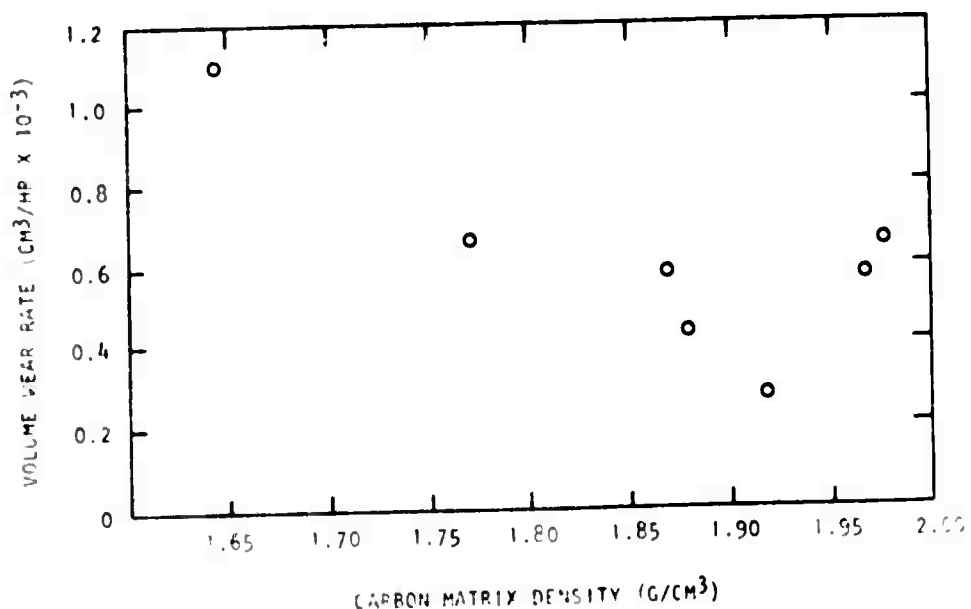


Fig. 28. Dependence of volume wear rate on carbon matrix density for alloyed carbons

5. PHYSICAL PROPERTIES

(K. Koyama and R. J. Price)

5.1. THERMAL EXPANSIVITY OF PURE PYROLYTIC CARBONS

The thermal expansivity of the pure isotropic pyrolytic carbons is being studied. Three strips of carbon measuring about 0.7 in. x 0.05 in. x 0.01 in. are enclosed in a special holder which allows the longitudinal expansion of the strips (parallel to the deposition plane) to be measured without the strips bending under load of the dilatometer pushrods. Other experimental details are given in Ref. 1.

The thermal expansivities of several carbons were reported in Ref. 1. During the current reporting period additional samples have been measured to extend the range of carbon densities investigated to 1.35 to 2.01 g/cm³. Measurements were made between room temperature and 1000°C. The deposition conditions and structural properties of all the carbons tested are listed in Table 8. The carbons included a series deposited from 60% propane at bed temperatures spanning the range 1140° to 1400°C, and a series deposited at 1330° to 1350°C with propane concentrations ranging from 3% to 60%.

The thermal expansivity curves show a slight upward curvature. Table 9 lists the mean CTE of the carbon between room temperature and 1000°C, and also the instantaneous CTE at 400°C and 1000°C. The difference between the latter two numbers is an indication of the upward curvature of the expansion curve.

Examination of the data in Tables 8 and 9 shows that the CTE of the carbons is principally controlled by the density. Figure 29 shows the mean CTE (22° to 1000°C) of the carbons plotted as a function of carbon density. The dependence is linear within the scatter of the data. The curvature of the thermal expansivity curve (indicated by the difference between instantaneous CTE at 400°C and that at 1000°C (Table 9) was greatest for the lowest

TABLE 8
DEPOSITION CONDITIONS AND STRUCTURAL PARAMETERS OF PYROLYTIC
CARBONS USED FOR MEASUREMENT OF THERMAL EXPANSIVITY

Deposition Run No.	CTE Run No.	Deposition Conditions			Structural Parameters	
		Propane Conc. (%)	Bed Temp (°C)	Average Coating Rate (mils/min)	Density (g/cm ³)	Apparent Crystallite Height, L _c (Å)
5408-7	J0476	60	1180	0.234	1.974	36
5408-11	J0477	7	1330	0.058	1.553	23
5408-23	J0478	7	1280	0.054	1.717	25
5408-25	J0479	60	1300	0.317	1.753	29
5408-27	J0480	25	1340	0.225	1.592	24
5408-31	J0481	60	1230	0.267	1.823	33
5408-33	J0482	60	1355	0.384	1.535	26
5408-35	J0483	60	1400	0.333	1.459	26
5408-19	K0025	60	1140	0.217	2.008	35
5408-17	K0026	3	1330	0.036	1.457	20
5408-29	K0283	7	1400	0.050	1.353	26

TABLE 9
THERMAL EXPANSIVITY OF PYROLYTIC CARBONS

Run No.	Density (g/cm ³)	Apparent Crystal Height, $\frac{\text{cm}}{\text{C}}$	Coefficient of Thermal Expansion ($10^{-6} \text{ }^{\circ}\text{C}^{-1}$)		
			Mean, 22°-1000°C	Instantaneous, 400°C	Instantaneous, 1000°C
5408-7	1.974	36	5.95	6.15	6.26
5408-11	1.553	23	4.40	4.46	4.75
5408-23	1.717	25	4.56	4.77	4.81
5408-25	1.753	29	5.36	5.40	5.77
5408-27	1.592	24	4.68	4.90	5.07
5408-31	1.823	33	5.62	5.75	6.02
5408-33	1.535	26	4.50	4.55	4.79
5408-35	1.459	26	4.08	4.27	4.57
5408-19	2.008	35	6.54	6.41	7.18
5408-17	1.457	20	3.97	4.21	4.80
5408-29	1.353	26	3.53	3.15	4.45

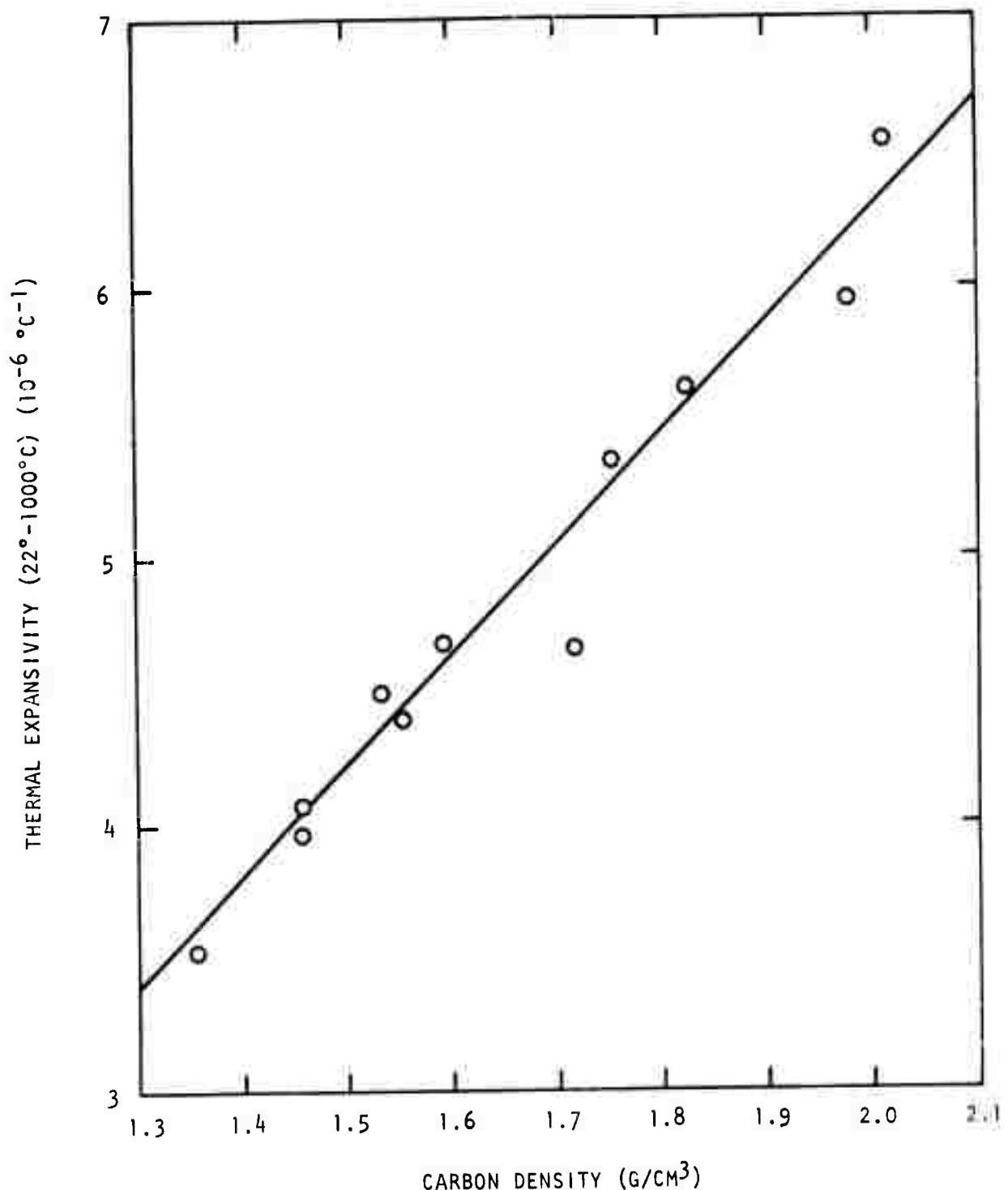


Fig. 29. Thermal expansivity of isotropic pyrolytic carbons as a function of carbon density

density carbon ($\rho = 1.353 \text{ g/cm}^3$), but there was no general correlation between curvature and carbon density.

Since the a-axis thermal expansion coefficient of a graphite crystal is zero at 400°C, the 400°C thermal expansivity of polycrystalline carbon or graphite is caused solely by the c-axis expansion of the crystallites. A linear CTE of $6.4 \times 10^{-6} \text{ }^\circ\text{C}^{-1}$ for the highest density carbon indicates a volumetric thermal expansivity of $\sim 19 \times 10^{-6} \text{ }^\circ\text{C}^{-1}$, which is equal to or slightly higher than the crystallite c-axis thermal expansivity reported by Pellegrini⁽¹⁷⁾ for fluidized bed pyrocarbons with a similar crystallite size (35 Å). This measurement suggests that the expansion of the crystallites in the highest density carbon is transmitted directly to the aggregate with no accommodation by pores or elastic constraints, in contrast to the considerable accommodation observed in most carbon and graphite artifacts.

5.2. THERMAL CONDUCTIVITY OF PURE PYROLYTIC CARBONS

The thermal conductivity of isotropic pyrolytic carbons is being studied by the heat-pulse method. When a short-duration heat pulse is flashed onto one face of a parallel-faced sample, the time lag for the rear-face temperature to rise to some specified fraction of its final value is related to the thermal diffusivity of the material.⁽¹⁸⁾ The measured thermal diffusivity may then be multiplied by the sample density and heat capacity to obtain the thermal conductivity. In the present work, thermal diffusivity readings are taken at 100°C intervals between room temperature and 800°C and converted to thermal conductivity by using heat capacity values taken from the literature.

Results for five pyrolytic carbons were reported in the previous report.⁽¹⁾ The heat capacity data used in the calculations were from measurements made about 10 years ago on massive, oriented pyrolytic carbons deposited from methane at around 2000°C.⁽¹⁹⁾ These measurements differ considerably from the accepted values for graphite, as shown in Fig. 30. However, recent measurements of the heat capacity of glassy carbons show little, if any, deviation from the graphite values.⁽²⁰⁾ Since isotropic pyrolytic carbons are closer

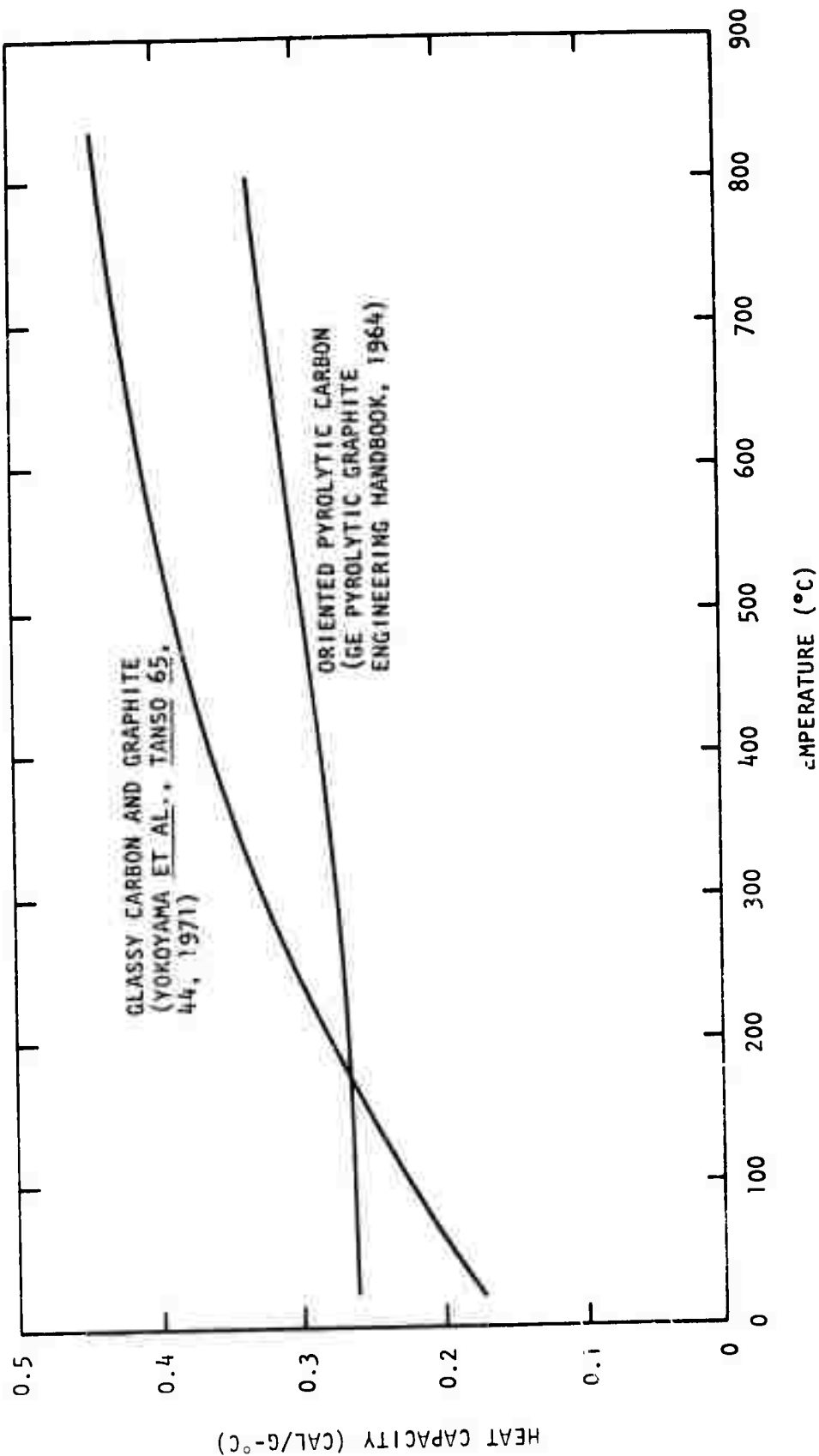


Fig. 30. Heat capacity of carbons and graphite as a function of temperature

structurally to glassy carbons than to oriented, massive pyrolytic carbon, it is probable that the recent measurements on glassy carbons should also be used for isotropic pyrolytic carbons in preference to the older, unconfirmed measurements on oriented pyrolytic carbon. The substitution of the new heat capacity data for the old makes a considerable difference in the calculated thermal conductivity measurements. Typical curves of thermal conductivity versus temperature, using both old and new heat capacity data, are shown in Fig. 31. It may be seen that using the new heat capacity data the temperature dependence is now similar to that of glassy carbons⁽²¹⁾ and other poorly crystalline carbons, with the thermal conductivity increasing with temperature up to ~500°C.

Measurements on all the carbons tested so far are listed in Table 10. The data for the five carbons reported in the previous report⁽¹⁾ have been corrected by using the new heat capacity data.

The thermal conductivity at 100°C is plotted as a function of density in Fig. 32 and as a function of apparent crystallite size (L_c) in Fig. 33. The thermal conductivity tends to increase with both these parameters (the highest density carbons, in general, have the largest crystallite sizes). However, the scatter in the data is considerably reduced when apparent crystallite height is used as the plotting parameter, indicating that the crystallite size is an important factor in controlling the thermal conductivity.

Thermal conduction in polycrystalline carbon or graphite takes place by phonon transport parallel to the layer planes. Kelly⁽²²⁾ has shown that at a temperature T the thermal conductivity, K_T , may be represented as follows:

$$\frac{1}{K_T} = \gamma \left[\frac{1}{(K_U)_T} + \frac{c_d s^2}{(c_d s^2 K_D)_T} + \frac{1}{L_a} \left(\frac{L_a}{K_B} \right)_T \right]$$

where γ is a porosity-tortuosity factor (always greater than 1), $(K_U)_T$ is the thermal conductivity component due to Umklapp processes at temperature T,

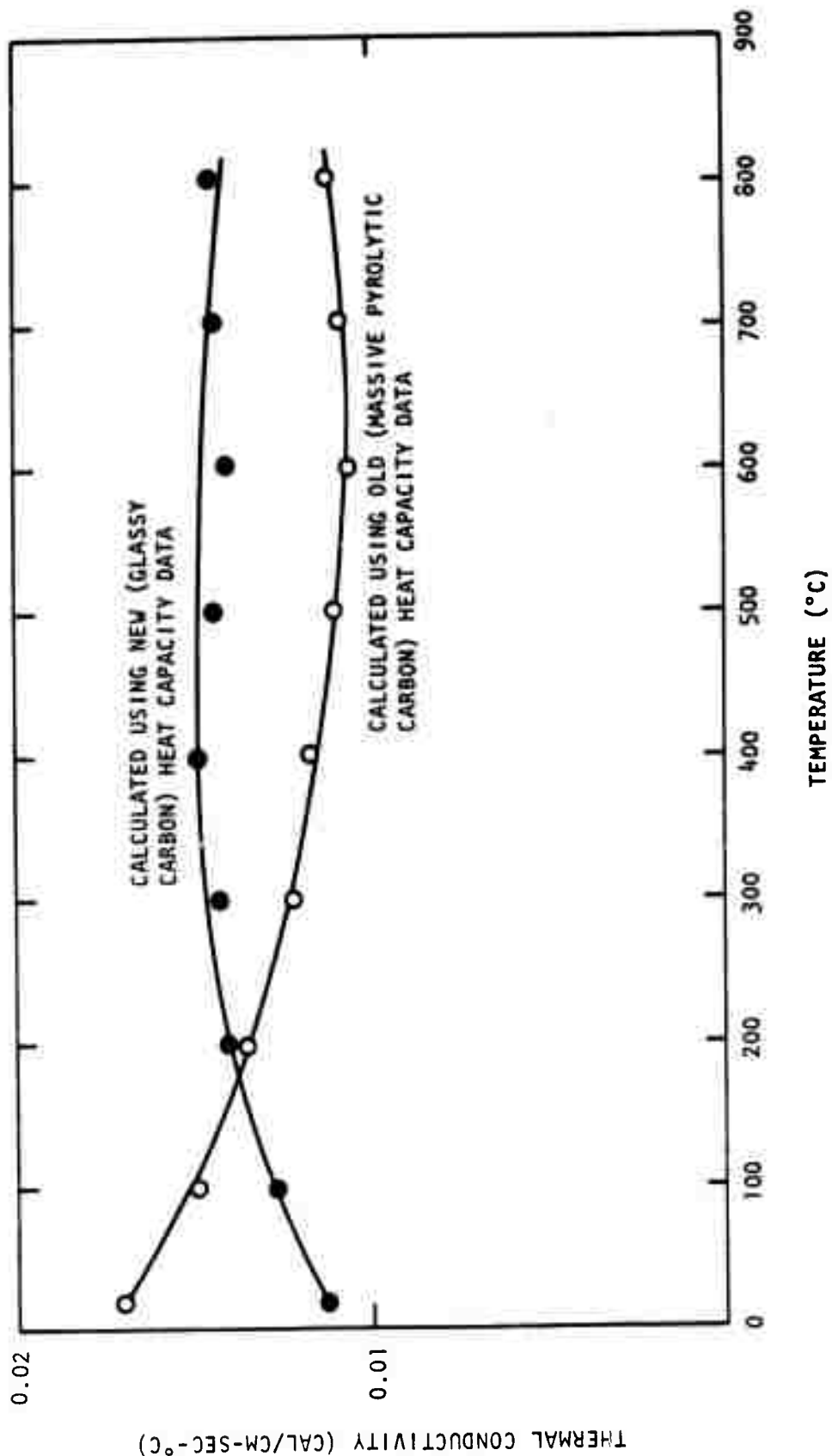


Fig. 31. Thermal conductivity of isotropic pyrolytic carbon (run 5408-25) as a function of temperature

TABLE 10
DEPOSITION CONDITIONS, STRUCTURAL PARAMETERS, AND THERMAL CONDUCTIVITY OF PYROLYTIC CARBONS

Deposition Run No.	Thermal Diffus. Run No.	Propane Conc. (%)	Bed Temp. (°C)	Average Coating Rate (mils/min)	Carbon Density (g/cm ³)	Apparent Crystallite Height, L _c (Å)	Thermal Conductivity (cal/cm ² sec ⁻¹ °C)				
							22°C	200°C	400°C	600°C	800°C
5408-7	K0001	60	1180	0.234	1.974	36	0.0133	0.0165	0.0177	0.0188	0.0188
5408-5	K0002	60	1300	0.317	1.753	29	0.0113	0.0141	0.0143	0.0140	0.0144
5408-27	K0003	25	1340	0.225	1.592	24	0.0100	0.0136	0.0139	0.0139	0.0135
5408-31	K0004	60	1230	0.267	1.823	33	0.0113	0.0152	0.0152	0.0155	0.0150
5408-33	K0005	60	1355	0.384	1.535	26	0.0094	0.0118	0.0133	0.0130	0.0124
5408-17	K0028	3	1330	0.036	1.457	20	0.0072	0.0093	0.0118	0.0126	0.0132
5408-19	K0029	60	1140	0.217	2.008	35	0.0100	0.0143	0.0156	0.0165	0.0185
5408-23	K0030	7	1280	0.054	1.717	25	0.0077	0.0114	0.0135	0.0130	0.0126
5408-29	K0031	7	1400	0.050	1.353	26	0.0088	0.0118	0.0136	0.0134	—
5408-11	K0032	7	1330	0.058	1.553	23	0.0092	0.0126	0.0140	0.0145	0.0149
5408-35	K0033	60	1400	0.333	1.459	26	0.0112	0.0146	0.0170	0.0163	0.0155

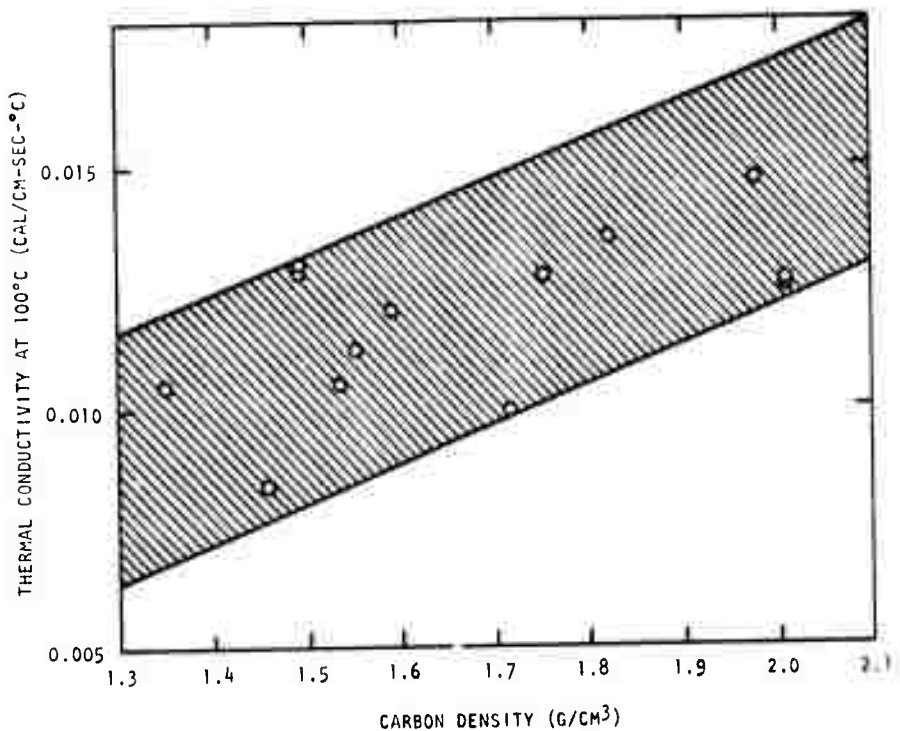


Fig. 32. Thermal conductivity at 100°C of isotropic pyrolytic carbons as a function of carbon density

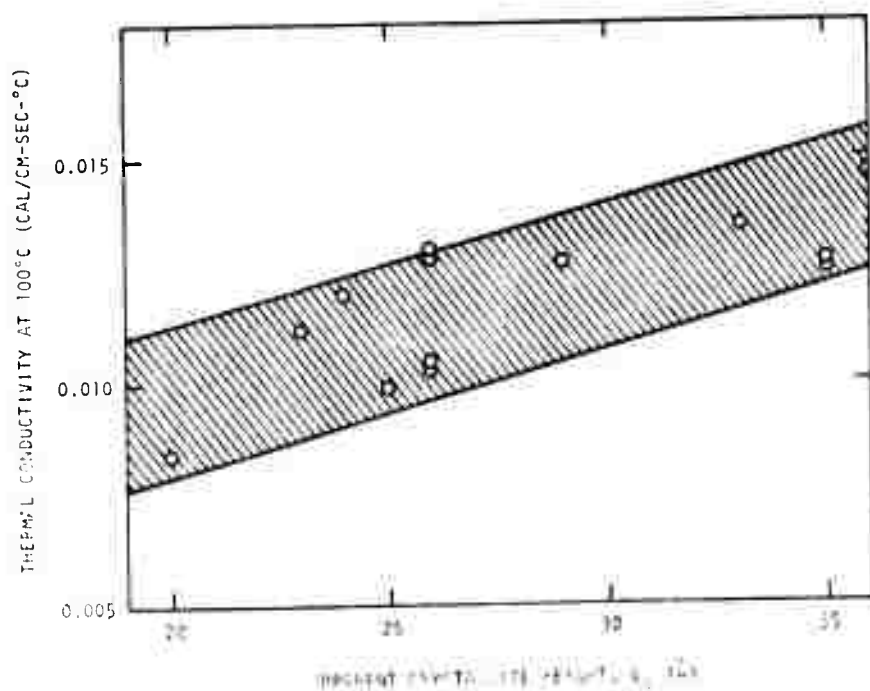


Fig. 33. Thermal conductivity at 100°C of isotropic pyrolytic carbons as a function of apparent crystallite height, L_c

C_d is the concentration of point defects, S^2 is a point defect scattering parameter, K_D is the thermal conductivity contribution for point defects, L_a is the phonon mean free path between crystallite boundaries, and K_B is the thermal conductivity component controlled by crystallite boundaries.

The $(K_U)_T$ value is known from measurements on well-annealed, highly oriented pyrolytic graphite and decreases with increasing temperature. The values for $(C_d S^2 K_D)_T$ and $(K_B/L_a)_T$ have been calculated; the former is almost independent of temperature, while the latter increases with increasing temperature. The different temperature dependences of the three components make it possible to calculate "best-fit" values for γ , $C_d S^2$, and L_a from curves of the thermal conductivity versus temperature.^(23,24) When the temperature-dependence curves are restricted to measurements above room temperature the results obtained from such an analysis are subject to considerable error (especially those for the point defect concentration), but the approximate values of γ and L_a may have significance in describing the thermal conduction mechanism.

The thermal conductivity data for the carbons listed in Table 10 were analyzed in the manner described above. Values for γ (the porosity-tortuosity factor) fell in the range 6 to 30, with most samples giving γ values around 20. The L_a values were in the range 100 to 300 Å. There was no obvious correlation between the individual values of γ and L_a and the corresponding structural parameters. A porosity-tortuosity factor of about 20 is consistent with a heat-conduction path in the isotropic pyrolytic carbons leading through the oriented outer layers of the "droplets" which comprise these materials. Transmission electron microscopy shows that these droplets have an "onion skin" structure with the layer planes tending to lie circumferentially.⁽⁷⁾ The L_a values of around 200 Å are considerably larger than the width of the coherently diffracting zones observed by electron microscopy, which are less than 50 Å wide.⁽⁷⁾ A possible explanation is that the diffracting zones observed by electron microscopy are bounded by low-angle boundaries which are transparent to phonons.

C_d is the concentration of point defects, S^2 is a point defect scattering parameter, K_D is the thermal conductivity contribution for point defects, L_a is the phonon mean free path between crystallite boundaries, and K_B is the thermal conductivity component controlled by crystallite boundaries.

The $(K_U)_T$ value is known from measurements on well-annealed, highly oriented pyrolytic graphite and decreases with increasing temperature. The values for $(C_d S^2 K_D)_T$ and $(K_B/L_a)_T$ have been calculated; the former is almost independent of temperature, while the latter increases with increasing temperature. The different temperature dependences of the three components make it possible to calculate "best-fit" values for γ , $C_d S^2$, and L_a from curves of the thermal conductivity versus temperature.^(23,24) When the temperature-dependence curves are restricted to measurements above room temperature the results obtained from such an analysis are subject to considerable error (especially those for the point defect concentration), but the approximate values of γ and L_a may have significance in describing the thermal conduction mechanism.

The thermal conductivity data for the carbons listed in Table 10 were analyzed in the manner described above. Values for γ (the porosity-tortuosity factor) fell in the range 6 to 30, with most samples giving γ values around 20. The L_a values were in the range 100 to 300 Å. There was no obvious correlation between the individual values of γ and L_a and the corresponding structural parameters. A porosity-tortuosity factor of about 20 is consistent with a heat-conduction path in the isotropic pyrolytic carbons leading through the oriented outer layers of the "droplets" which comprise these materials. Transmission electron microscopy shows that these droplets have an "onion skin" structure with the layer planes tending to lie circumferentially.⁽⁷⁾ The L_a values of around 200 Å are considerably larger than the width of the coherently diffracting zones observed by electron microscopy, which are less than 50 Å wide.⁽⁷⁾ A possible explanation is that the diffracting zones observed by electron microscopy are bounded by low-angle boundaries which are transparent to phonons.

5.3. THERMAL CONDUCTIVITY OF SILICON-ALLOYED PYROLYTIC CARBONS

The thermal diffusivity of five silicon-alloyed pyrolytic carbons containing between 4 and 28 wt-% silicon was measured by the heat-pulse method. The thermal conductivity was obtained by multiplying by the sample density and the heat capacity. The heat capacity was calculated from the fractions by weight of silicon carbide and carbon, and literature values for the heat capacity of silicon carbide⁽²⁵⁾ and glassy carbon.⁽²⁰⁾

The results are listed in Table 11. The temperature dependence of the thermal conductivity is similar to that of pure carbon. The thermal conductivity at 100°C is plotted as a function of apparent crystallite height, L_c , in Fig. 34; the data band for pure carbons is shown on the same figure. It may be seen that the conductivity of the silicon-alloyed carbons is consistently lower than that of the pure carbons. There is no clear dependence on the silicon content.

Since the thermal conductivity of pyrolytic β -silicon carbide⁽²⁶⁾ is about ten times higher than that of low-temperature isotropic pyrolytic carbons, it is evident that the thermal conductivity of the alloyed carbons is controlled by the carbon phase and is not improved by the presence of substantial amounts of silicon carbide. The shape of the conductivity-versus-temperature curves, which rises with increasing temperature up to $\sim 500^\circ\text{C}$ while that of pyrolytic silicon carbide decreases over the same range,⁽²⁶⁾ confirms that the carbon controls the heat conduction process.

The reduction of the thermal conductivity below that of pure carbons (Fig. 32) requires explanation. Kelly *et al.*⁽²⁷⁾ found that the addition of about 0.5 wt-% boron to polycrystalline graphite reduced the room-temperature thermal conductivity by 30 to 50%. The reduction was attributed to the scattering of phonons by the substitutional boron atoms. The solubility of silicon in carbon has not been directly measured, but indirect evidence suggests that up to 0.15 to 0.2 wt-% silicon may enter the carbon as a substitutional solid solution.⁽²⁸⁾

TABLE 11
DEPOSITION CONDITIONS, STRUCTURAL PARAMETERS, AND THERMAL CONDUCTIVITY OF SILICON-ALLOYED PYROLYTIC CARBONS

Deposition Run No.	Thermal Diffus. Run No.	Deposition Conditions		Structural Parameters		Thermal Conductivity (cal/cm-sec-°C)					
		Propane Conc. (%)	Bed Temp (°C)	Silicon Content (wt-%)	Carbon Density (g/cm ³)	Apparent Crystallite Height, L _c (Å)	22°C	200°C	400°C	600°C	800°C
5408-87	K0301	7	1290	23.0	1.88	35	0.0067	0.0087	0.0095	0.0099	0.0100
5408-69	K0300	25	1270	15.0	1.92	35	0.0050	0.0067	0.0075	0.0085	0.0088
5408-61	K0298	7	1340	28.0	1.77	38	0.0073	0.0086	0.0100	0.0102	0.0099
5408-57	K0297	60	1295	9.5	1.98	39	0.0088	0.0117	0.0130	0.0136	—
5408-67	K0299	60	1350	4.0	1.98	48	0.0127	0.0160	0.0185	0.0190	0.0186

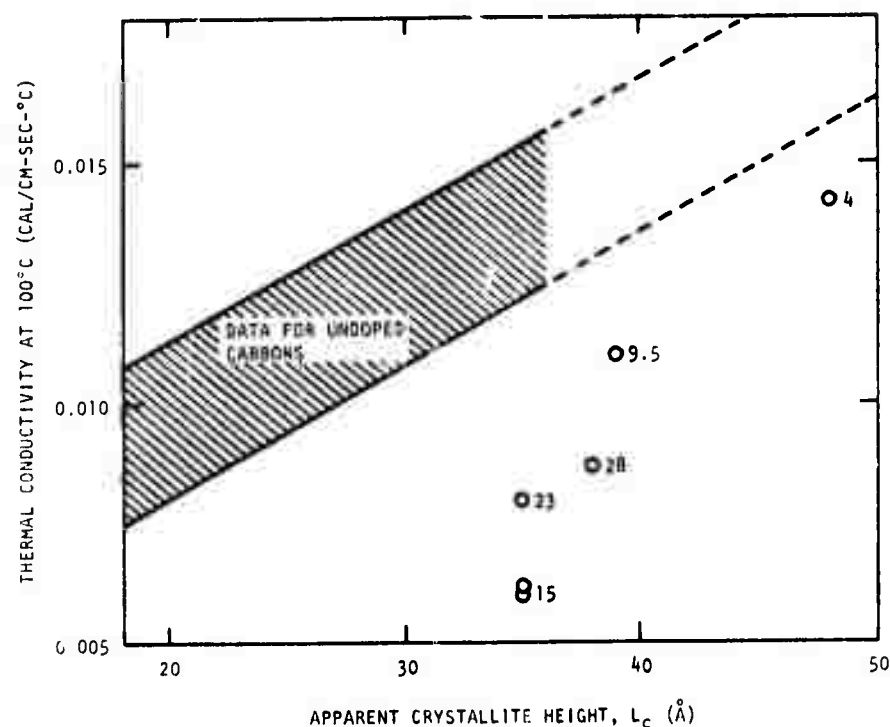


Fig. 34. Thermal conductivity at 100°C of silicon-alloyed pyrolytic carbons as a function of L_c . The numbers beside the points represent the percentage by weight of silicon

The change in thermal resistivity resulting from the introduction of additional point defects is given by:

$$\Delta \left(\frac{1}{K_T} \right) = \gamma \left[\frac{C_d S^2}{(C_d S^2 K_D)_T} \right]$$

where the meaning of the symbols is the same as in Section 5.2. Because of the scatter in the data, it is difficult to assign a definite value to $\Delta(1/K_T)$. The data in Fig. 34 suggest that for carbons with $L_c \approx 35 \text{ \AA}$ the introduction of silicon reduces K at 100°C from about $0.014 \text{ cal/cm-sec-}^\circ\text{C}$ to about $0.008 \text{ cal/cm-sec-}^\circ\text{C}$. Thus, $\Delta(1/K)$ would be about $50 \text{ cm-sec-}^\circ\text{C/cal}$. Using a value of 20 for γ (see Section 5.2) and $3 \times 10^{-3} \text{ cal/cm-sec-}^\circ\text{C}$ for $(C_d S^2 K_D)$ (Ref. 23), a value of 7×10^{-3} is obtained for $C_d S^2$. For a silicon solubility of 0.2 wt-%, the point defect concentration, C_d , would be about 10^{-3} , and the point defect scattering parameter, S^2 , would be ~ 7 . This is considerably higher than the value of 0.3 obtained for a substitutional boron atom,⁽²⁷⁾ but it may be a reasonable value in view of the greater difference in mass between a silicon and carbon atom compared with the difference between a boron and a carbon atom.

REFERENCES

1. Akins, R. J., et al., "Semiannual Technical Report for the Period 1 July 1971 to 31 December 1971, Carbon Research," Gulf-EL-A10968, Gulf Electronics Systems Division, Gulf Energy & Environmental Systems Company, January 31, 1972.
2. Frantz, J. F., "Minimum Fluidization Velocities and Pressure Drop in Fluidized Beds," paper presented at 57th Annual Meeting, A.I.Ch.E., Boston, Mass., December 6-10, 1964 (P/38).
3. Bokros, J. C., Carbon 3, 201 (1965).
4. Kaae, J. L., J. Nucl. Mater. 38, 42 (1971).
5. Kaae, J. L., Carbon 9, 291 (1971).
6. Kaae, J. L., J. Biomed. Mater. Res. 6, 279 (1972).
7. Kaae, J. L., et al., "Transmission Electron Microscopy of Pyrolytic Carbons Deposited in a Bed of Fluidized Particles," Gulf-GA-A10931, Gulf General Atomic, January 1972.
8. Gulden, T. D., "Stacking Faults in Chemically Vapor-Deposited β -SiC," GA-10466, Gulf General Atomic, February 1971.
9. Ban, L. L., and W. M. Hess, "Microstructure of Carbons," paper presented at the Tenth Biennial Conference on Carbon, Bethlehem, Pa., June 1971.
10. Conway, H. D., Phil. Mag. 38, 905 (1947).
11. Price, R. J., and J. L. Kaae, Carbon 7, 706 (1969).
12. Leichter, H. L., and E. Robinson, J. Am. Ceram. Soc. 53, 197 (1970).
13. Barabanov, V. N., et al., Ind. Lab. 32, 459 (1964).
14. Green, L., Jr., J. Appl. Mech. 18, 345 (1951).
15. Tsuzuku, T., Carbon 1, 25 (1963).
16. Tsuzuku, T., Carbon 1, 511 (1964).
17. Pellegrini, G., M. Moulaert, and I. Zubani, paper presented at the Tenth Biennial Conference on Carbon, Bethlehem, Pa., June 1971.
18. Parker, W. J., et al., J. Appl. Phys. 32, 1679 (1961).
19. Pyrolytic Graphite Engineering Handbook, Metallurgical Products Department, General Electric Company, Detroit, Michigan, 1964.

20. Yokoyama, J., et al., Tanso 65, 44 (1971).
21. Tingey, G. L., et al., "Semiannual Technical Report for the Period 2 November 1971 to 1 May 1972, Investigation of the Influence of Structure on the Chemical Stability and Thermal/Mechanical Shock Properties of Glass-Like Carbons," BNW No. 211B00718, June 1972.
22. Kelly, B. T., Chem. Phys. Carbons 5, 119 (1969).
23. Taylor, R., et al., Carbon 6, 537 (1968).
24. McNerney, S., and B. T. Kelly, Proceedings, 3rd Conference on Industrial Carbon and Graphite, Society of Chemical Industry, London, 1971, p. 36.
25. Thermophysical Properties of High-Temperature Solid Materials, Y. S. Touloukian (ed.) v. 5, Macmillan Co., New York, 1967, p. 123.
26. Price, R. J., Am. Ceram. Soc. Bull. 48, 859 (1969).
27. Kelly, B. T., et al., Carbon 9, 447 (1971).
28. Marinkovic, S., et al., Carbon 8, 283 (1970).

APPENDIX A
WORK STATEMENT

The work statement for the current contract year is:

- "a. The Contractor shall use its best efforts to investigate the control of the structure of carbonaceous materials in the basic deposition process in fluid beds. Catalysts will be used to manipulate the deposition process and additives will be co-deposited with the carbon to expand the number of structures attainable. The structure of the deposited carbon will be related to the deposition conditions and variations in properties will be interpreted in terms of the structure.
- b. During this contract term, major emphasis will be devoted to investigating deposition in steady-state beds and characterizing the structures that are formed. The primary goal will be to develop an understanding of the deposition mechanism and the structures formed so that the structure deposited may be controlled at will through appropriate adjustments of the pyrolysis conditions.
- c. In determining whether or not the Contractor has performed with due diligence hereunder, it is agreed and understood that the Contracting Officer may measure the amount and quality of the Contractor's efforts against the representations made by the Contractor in negotiation of this contract and as contained in the Contractor's Proposal GGAP 11-043, dated 9 February 1971, a copy of which is on file in the office of the Contracting Officer."

Unclassified

Security Classification

DOCUMENT CONTROL DATA - R & D

(Security classification of title, body of abstract and indexing annotation must be entered when the overall report is classified)

1. ORIGINATING ACTIVITY (Corporate author)

Gulf Oil Corporation
 Gulf Energy & Environmental Systems Company
 P.O. Box 608, San Diego, California 92112

2a. REPORT SECURITY CLASSIFICATION

Unclassified

2b. GROUP

3. REPORT TITLE

Carbon Research

4. DESCRIPTIVE NOTES (Type of report and inclusive dates)

Semianual January 1, 1972 - June 30, 1972

5. AUTHOR(S) (First name, middle initial, last name)

Jack C. Bokros, Robert J. Akins, James L. Kaae, Karl (NMI) Koyama, Robert J. Price,
 Frederick J. Schoen

6. REPORT DATE

August 25, 1972

7a. TOTAL NO. OF PAGES

83

7b. NO. OF REFS

28

8a. CONTRACT OR GRANT NO

DAHC15-71-C-0282

8b. ORIGINATOR'S REPORT NUMBER(S)

Gulf-EL-A12250

8c. PROJECT NO.

c.

d.

9b. OTHER REPORT NO(S) (Any other numbers that may be assigned this report)

10. DISTRIBUTION STATEMENT

Approved for public release; distribution unlimited.

11. SUPPLEMENTARY NOTES

12. SPONSORING MILITARY ACTIVITY

Advanced Research Projects Agency
 Washington, D.C.

13. ABSTRACT

Although the pyrolytic carbons deposited in fluid beds have structures and properties that can be varied over wide ranges, technological advances have been slow to develop. This is due to the lack of well-defined relations between the structure and properties of these carbons and to a poor understanding of the deposition process. The primary objective of this program is to provide the deposition-structure-property relations that are needed for expanded technological utilization.

During the first six months, several exploratory fields of structures were deposited using steady-state beds. Studies of these deposits revealed that the realization of the full-strength potential was not being achieved because of the presence of soot inclusions in the microstructure. Although improvements have been made by increasing the exit gas velocity and increasing the bed surface area, further improvement is desired. For this purpose, methane, a more stable hydrocarbon, is being used in the deposition.

X-ray data characterizing the carbon-silicon alloys that were deposited in the initial six-month period show that, contrary to the pure carbons, the crystallinity (the L_c parameter) of the silicon-alloyed carbons increases with increasing deposition temperature in the range 1150° to 1400°C. The trend toward larger L_c values with increasing propane concentrations is the same as for pure carbons, and is consistent with the suggested theory for carbon deposition in fluidized beds. Since carbon-silicon alloys with smaller L_c values are harder than alloys with larger values, stronger deposits are likely to be attained using higher propane and silicon concentrations and lower deposition temperatures.

14. KEY WORDS	LINK A		LINK B		LINK C	
	ROLE	WT	ROLE	WT	ROLE	WT
Pyrolytic carbons Fluidized beds Steady-state fluidized beds Chemical vapor deposition Pyrolytic-carbon wear properties Pyrolytic-carbon fatigue properties Pyrolytic-carbon strength properties Pyrolytic-carbon physical properties Silicon-alloyed pyrolytic carbons						

13. Abstract (Continued)

A new injector system has been developed and tested which allows independent control of methyltrichlorosilane and hydrocarbon that can be metered into the fluidized bed. This will expand the number of structures that can be deposited. In particular, this control will provide the means for depositing silicon-carbon alloys with both high silicon concentration and high carbon matrix density.

Thin sections, both parallel and perpendicular to the deposition plane, of pure and silicon-alloyed isotropic pyrolytic carbons were examined by transmission electron microscopy to observe the fine-scale structural features. A low-density carbon ($\rho = 1.55 \text{ g/cm}^3$) contained spherical growth features separated by pores. The spherical features, which are believed to originate with droplets of high-molecular-weight hydrocarbons during deposition, consisted of a relatively dense central nucleus surrounded by a less dense region containing crystallites whose form suggests tangled "tendrils." A high-density carbon ($\rho = 1.97 \text{ g/cm}^3$) also contained spherical structural features with central nuclei, but with edges that tended to be flattened and with smaller intervening pores. An isotropic carbon containing 8 wt-% silicon contained a uniform dispersion of $\sim 100\text{-}\text{\AA}$ particles of silicon carbide, whereas a sample containing 34 wt-% silicon had a heterogeneous structure in which spherical growth features free from silicon carbide alternated with regions containing a high density of silicon carbide platelets.

Strips of isotropic pyrolytic carbons deposited in steady-state fluidized beds were tested in three-point bending. The moduli of rupture were somewhat higher than those previously measured in four-point bending, particularly when a very small knife-edge spacing was used. However, the moduli of rupture were still significantly lower than for similar carbons deposited in non-steady-state beds. The modulus of rupture of a carbon deposited under conditions intended to minimize soot formation was not significantly different from that of carbon deposited under standard conditions.

A low-density and a medium-density carbon were fatigue-tested at 1800 cpm using cantilever beam specimens. With peak stresses greater than 90% of the mean single-cycle fracture stress, most samples survived 10^5 cycles without failure and some had not failed after 10^7 cycles. Thus, the endurance limit for these carbons is very close to the single-cycle fracture stress.

Wear data developed during the past six months indicate that under a fixed test situation, the wear rate varies with structure over two orders of magnitude. The wear resistance of low density (1.50 g/cm^3) isotropic pyrolytic carbon and that of glassy carbon (density = 1.50 g/cm^3) are similar and low. The highest wear resistance was exhibited by the silicon-alloyed pyrolytic carbons. Wear caused by pure titanium rubbing on carbon was catastrophic.

The in-plane thermal expansivity was measured for a series of isotropic pyrolytic carbons with densities ranging from 1.35 to 2.01 g/cm^3 . The expansivity increased linearly with the carbon density and reached a value of $6.4 \times 10^{-6} \text{ }^\circ\text{C}^{-1}$ (at 400°C) for a carbon with a density of 2.01 g/cm^3 .

Thermal conductivities of isotropic pyrolytic carbons are being obtained from the thermal diffusivities measured by the heat-pulse method. Recent literature values for the heat capacity of glassy carbon are being used to convert the thermal diffusivities to conductivities. Conductivities previously reported under this program are now believed to be in error due to the use of obsolete heat capacity data for massive, oriented pyrolytic carbon.

13. Abstract (Continued)

The new values show the thermal conductivity of the carbons increasing with increasing measurement temperature up to $\sim 500^{\circ}\text{C}$. The thermal conductivity of the carbons correlates better with apparent crystallite size, L_c , than with the density. The conductivity increases with increasing L_c . Analysis of the thermal conductivity-versus-temperature curves indicates that the heat conduction path is tortuous and that the mean spacing of phonon-scattering crystallite boundaries is 100 to 300 Å.

The thermal conductivity of pyrolytic carbons containing 4 to 28 wt-% silicon is lower than that of pure carbon but shows a similar temperature dependence. The thermal conductivity of the alloyed carbons is evidently controlled by the carbon phase and may be affected by a small amount of substitutionally dissolved silicon.